PHYSICAL REVIEW FLUIDS **8**, 104301 (2023)

Inertial settling of an arbitrarily oriented cylinder in a quiescent flow: From short-time to quasisteady motion

Jean-Lou Pierson[*]
IFP Energies Nouvelles, Rond-point de l'échangeur de Solaize, 69360 Solaize, France

(Received 28 March 2023; accepted 6 September 2023; published 10 October 2023)

In this article, we investigate the inertial settling of an arbitrarily oriented cylinder settling under gravity. We focus on two regimes: the very short-time and long-time dynamic. Using the generalized Kirchhoff equations to describe the particle motion, we demonstrate that during the very short dynamic regime, a cylinder starting from rest behaves with sedimenting velocities and angular velocity proportional to t and t^3, respectively. We then explore the long-time behavior and evaluate the validity of the quasisteady assumption under which the fluid unsteady term can be neglected. Using a dimensional analysis, we establish that the quasisteady assumption only applies to regimes where the Reynolds number is much smaller than 1. However, by comparing the results of quasisteady models to recent experiments and direct numerical simulations, we demonstrate that this assumption is valid for a broader range of Reynolds numbers, particularly for long fibers. We also analyze the effect of particle inertia, and we show that it plays no significant role in the magnitude of the sedimenting velocities and angular velocity. However, for sufficiently large inertia, we reveal that the quasisteady model takes the form of a damped oscillator when the particle approaches its equilibrium position, which is broadside onto its direction of motion. We discuss the relevance of this solution in light of direct numerical simulations.

DOI: 10.1103/PhysRevFluids.8.104301

I. INTRODUCTION

The settling of anisotropic particles is a common occurrence in various environmental flows, such as the fall of microplastics in the ocean [1] or the precipitation of ice crystals in the atmosphere [2,3]. Despite its practical significance, the accurate modeling of anisotropic particle settling in turbulent or quiescent environments is challenging due to the coupling between the particle motion and the surrounding fluid flow. Unlike spherical particles, the orientation of the body has a significant impact on the rate of sedimentation. For example, in Stokes flow and for slender particles, the sedimentation velocity of a particle with its axis aligned with gravity is twice that of a particle with its axis perpendicular [4]. Additionally, the body's orientation is coupled to the translational equation of motion for inertial flows due to a nonzero hydrodynamic torque [5]. This results in an unsteady problem, as the body's orientation can change over time in response to torques. In this article, we examine the settling of a cylindrical particle in a quiescent flow as a first step in understanding the effect of an anisotropic shape on particle motion.

The most general equations for studying the gravitational settling of a single body in a quiescent fluid are the generalized Kirchhoff equations originally derived by Howe [6]. Under this framework, added mass and vorticity contributions to the hydrodynamic forces and torque are nonambiguously separated. However, for most configurations of practical interest, the vorticity contributions cannot be expressed in closed form as they depend on fluid motion history [7]. In the limit of negligible

---

[*] jean-lou.pierson@ifpen.fr

inertia and for a spherical particle translating and rotating, the force and torque can be decomposed into a quasisteady component and a history term that takes the form of integrodifferential equations [8]. There is no equivalent analytical formula for arbitrary axisymmetric particles, particularly cylinders. The explanation lies in the complexity of the history term for a nonspherical body, whose expression in the frequency domain is often too complicated to allow a closed-form expression in the time domain [9,10]. Moreover, unlike spherical particles, nonspherical particles have distinct high- and low-frequency expressions for the history term [11].

The situation is even worse for finite Reynolds numbers, for which few results exist for nonspherical particles for quasisteady and history loads. In Stokes flow, due to the reversibility of the Stokes equation, an axisymmetric particle with fore-aft symmetry embedded in a uniform flow of velocity U experiences no torque. In contrast, a torque that scales as U^2 appears in flow with small but finite inertia [5,12]. This torque naturally induces a coupling between translation and rotation for a sedimenting cylinder. Hence as a cylinder sediment in a fluid with non-negligible inertia, it rotates toward its equilibrium orientation, which is broad-side on to its direction of motion [12]. There is another nonlinear coupling term in the force balance for a rotating and translating axisymmetric body with fore-aft symmetry which scales as ΩU, where Ω is the angular velocity [5]. This term is at the origin of the lift force on a spinning sphere translating perpendicularly to its rotation axis [13]. This coupling term has not been studied so far in the context of a rotating cylinder settling perpendicular to its rotation axis. The history loads for nonspherical particles in the inertial regime have also received limited attention, with only a few studies providing force expressions for arbitrarily shaped particles in the long-time limit [14]. These expressions require knowledge of the steady velocity field created by the particle in Stokes flow, which is unknown for a moderately long cylinder. Nevertheless, scaling arguments indicate a t^{-2} long-time decay of the history force in the finite-inertia regime and a slower $t^{-1/2}$ decay in the Stokes regime [14].

Based on the previous literature review, making analytical progress without additional assumptions is challenging, primarily due to the absence of closed-form expressions for the history terms and ΩU load contribution. The quasisteady assumption introduced by Cox [5] assumes that the unsteady terms related to fluid motion are negligible. Through a scaling analysis, Cox [5] demonstrated that this assumption is appropriate as long as the Reynolds number based on the body length is much smaller than unity. This assumption has been used in various practical configurations, including the settling of fibrous aerosols in quiescent air [15] and fibers in liquids [16], yielding satisfactory results compared to experiments. Also, in those applications, the Reynolds number was not necessarily small. Shin *et al.* [17] have even shown that the quasisteady theory remains accurate for a Reynolds number based on the body length close to 1. Most prior studies [15,16] have made use of the quasisteady loads derived by Khayat and Cox [12] for slender fibers and the leading-order hydrodynamic torque resisting rotation provided by the slender body theory [4]. Recent research has shown that the lift force and inertial torque provided by Khayat and Cox [12] and the leading-order expression for the hydrodynamic torque resisting rotation are not accurate for moderately long rods [18,19], in line with the qualitative but nonquantitative agreement reported by Cabrera *et al.* [20] between the Khayat and Cox [12] theory and their experiments for moderately long rods. Hence, the validity of the quasisteady assumption must be reevaluated with accurate formulas for the loads. Additionally, the effect of the inertial correction to the loads proportional to ΩU must be considered. Scaling analyses by Cox [5] and Pierson *et al.* [18] have shown that this term may be small compared to the U^2 contribution when the inertia effects are not significant. However, the magnitude of this term for moderate inertia remains a topic of debate [18].

There is another limit where analytical progress is possible. In the limit of time shorter than the viscous timescale, added mass effects dominate over viscous contribution [21]. In this limit, the equations of motion can be solved, provided that the added mass loads are known. Loewenberg [9] has established the added mass forces on a cylindrical particle using potential flow solutions. However, the added mass torque for a rotating cylinder has no known solution.

The primary objective of this article is to address two critical issues in the study of an arbitrarily oriented cylinder settling under gravity. First, we provide analytical solutions to the problem in

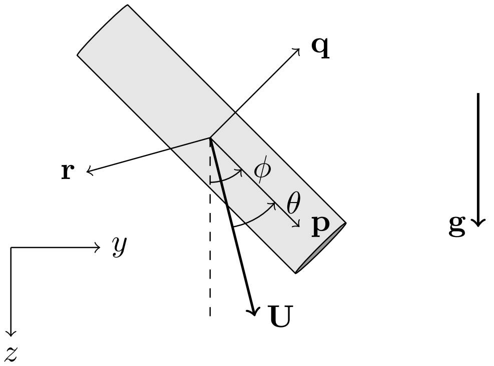

FIG. 1. Finite-length cylinder submitted to the gravity acceleration **g**.

the short-time limit where the added mass effects dominate. Secondly, we investigate the validity range of the quasisteady assumption and the neglect of the ΩU load contribution as a function of the relevant dimensionless parameters. These parameters include the cylinder aspect ratio, the Archimedes number (which is a Reynolds number based on gravitational velocity), and the density ratio. We perform the analysis using the generalized Kirchhoff equations as proposed by Howe [6] and Mougin and Magnaudet [21], and the quasisteady load expressions derived by Fintzi *et al.* [19], Pierson *et al.* [18] for moderately long rods, and Khayat and Cox [12] for very elongated fibers. We validate the proposed model through scaling analysis, experimental measurements from Roy *et al.* [16] and Cabrera *et al.* [20], and direct numerical simulations. The article is structured as follows. The governing equations are presented in Sec. II. Section III describes the analytical solutions in the short-time limit. The quasisteady models are derived in Sec. IV. The comparison between the quasisteady models and experimental measurements from Roy *et al.* [16] and Cabrera *et al.* [20] as well as direct numerical simulations are discussed in Sec. V. Section VI contains a discussion on the validity of the quasisteady model and our conclusions.

II. GOVERNING EQUATIONS

We consider a finite-length cylinder of length L and diameter D settling under gravity with velocity $\mathbf{U}$ and angular velocity $\mathbf{\Omega}$ (Fig. 1). We use the symbol $\mathbf{g}$ to represent the acceleration due to gravity, μ to denote the fluid viscosity, and ρ to represent the fluid density. Three dimensionless parameters may be defined: the aspect ratio $\chi = L/D$, the density ratio $\bar{\rho} = \rho_p/\rho$, and the Archimedes number $\mathrm{Ar} = (\rho_p - \rho)\rho g D^3/\mu^2$. Alternatively, to quantify the influence of particle inertia relative to viscous effects, we define the Stokes number as $\mathrm{St} = \bar{\rho}\mathrm{Ar}^2$.

The main difficulty in studying this problem is the coupling between the body motion and the surrounding flow field, which satisfies Navier-Stokes equations [7]. The equations of motion expressed in a reference frame having their origin fixed with respect to the laboratory, but axes rotating with the body read [6,21]

$$(m\mathbb{I} + \mathbb{A})\frac{d\mathbf{U}}{dt} + \mathbf{\Omega} \times [(m\mathbb{I} + \mathbb{A})\mathbf{U}] = \mathbf{F}^{\omega} + (m - \rho V)\mathbf{g}, \tag{1}$$

$$(\mathbb{J} + \mathbb{D})\frac{d\mathbf{\Omega}}{dt} + \mathbf{\Omega} \times [(\mathbb{J} + \mathbb{D})\mathbf{\Omega}] + \mathbf{U} \times (\mathbb{A} \times \mathbf{U}) = \mathbf{T}^{\omega}, \tag{2}$$

where m and V are, respectively, the cylinder mass and volume, $\mathbb{I}$ is the identity matrix, $\mathbb{J}$ is the inertia tensor, and $\mathbb{A}$ and $\mathbb{D}$ are the second-order added inertia tensors. All those tensors can be written using indicial notation as $J_{ij} = J_p p_i p_j + J_q(\delta_{ij} - p_i p_j)$, $A_{ij} = A_p p_i p_j + A_q(\delta_{ij} - p_i p_j)$, and $D_{ij} = D_q(\delta_{ij} - p_i p_j)$, where $\mathbf{p}$ is the unit orientation vector and $\mathbf{q}$ is the unit vector perpendicular to $\mathbf{p}$ in the plane (y, z) (Fig. 1). If the components of the inertia tensor can be readily obtained in a closed form for a finite-length cylinder [$J_p = mD^2/8$, $J_q = m(3D^2/4 + L^2)/12$], this is not the case for the components of the added mass tensors A_p, A_q, and D_q. If A_p and A_q have already been studied in the literature [9], to the best of the author's knowledge, no expression for D_q has been published yet. Based on the direct numerical simulation results of Kharrouba [22] and the potential flow results of Loewenberg [9], we derive correlations for A_p, A_q, and D_q in Appendix A. In Eqs. (1) and (2), $\mathbf{F}^\omega$ and $\mathbf{T}^\omega$ are the force and torque due to the vorticity in the flow. Except in inertia-dominated regimes, the motion of the cylinder is planar in the (p, q) plane [20], and the equation of motion simplifies to

$$(m + A_p)\frac{dU_p}{dt} - (m + A_q)\Omega_r U_q = F_p^\omega + (m - \rho V)g\cos\phi, \tag{3}$$

$$(m + A_q)\frac{dU_q}{dt} + (m + A_p)\Omega_r U_p = F_q^\omega - (m - \rho V)g\sin\phi, \tag{4}$$

$$(J_q + D_q)\frac{d\Omega_r}{dt} = -U_p U_q (A_q - A_p) + T_r^\omega. \tag{5}$$

The physical origin of the torque can be exemplified by looking more closely at Eq. (5). In steady potential flow, a torque manifests on a cylindrical particle as indicated by the first term on the right-hand side of Eq. (5) [23]. As the aspect ratio, χ, exceeds 1, $A_q > A_p$ (see Appendix A), and the torque is positive, orienting the body broad-side on. As a result, to leading order the torque expression provided by Khayat and Cox [12] for small Reynolds number and large aspect ratio ($\chi \gg 1$) $T_r = -5\pi/24\rho U_p U_q L^3/\ln^2(\chi)$ is the sum of two positive contributions due to potential flow and vorticity. For $\chi \gg 1$ the potential contribution $-U_p U_q (A_q - A_p)$ scales as $-\rho\pi D^2 U_p U_q L$ and is thus negligible to leading order in comparison to the vorticity contribution. The situation is less obvious for moderately large aspect ratio ($\chi \approx 2$) for which both contributions may have the same order of magnitude since the total torque on the body does not scale as $\rho U_p U_q L^3/\ln^2(\chi)$ [19].

III. SHORT-TIME DYNAMICS

Potential flow effects dominate over viscous effects in the high-frequency limit or equivalently for timescales shorter than the diffusive scale. This assertion may be proved by deriving the unsteady loads in the Stokes regime [10], but also by performing a short time analysis of the Navier-Stokes equation [21]. The latter is more general as it is not limited to the Stokes flow regime. The proper lengthscale to be used in the diffusive scale for the problem at hand is unknown *a priori*. However, Kabarowski and Khair [10] have shown that for both transverse and longitudinal oscillations, the added mass contributions dominate over the history load if $t \ll D^2/\nu$. Hence, the proper lengthscale in the short dynamic is the cylinder diameter, at least in the Stokes flow regime. Assuming $t \ll D^2/\nu$, Eqs. (3)–(5) simplify to

$$(m + A_p)\frac{dU_p}{dt} - (m + A_q)\Omega_r U_q = (m - \rho V)g\cos\phi, \tag{6}$$

$$(m + A_q)\frac{dU_q}{dt} + (m + A_p)\Omega_r U_p = -(m - \rho V)g\sin\phi, \tag{7}$$

$$(J_q + D_q)\frac{d\Omega_r}{dt} = -U_p U_q (A_q - A_p), \tag{8}$$

$$\frac{d\phi}{dt} = \Omega_r, \tag{9}$$

where we made explicit the equation ruling the dependency of ϕ with time. There is no closed-form analytical solution to this nonlinearly coupled system of equations, although there is a straightforward analytical treatment in the case of zero gravity [24]. We must solve this system numerically, but one may get insightful estimates using asymptotic analysis. By balancing the acceleration of gravity with the particle acceleration in Eqs. (6) and (7), we obtain $U \sim gT$, where U is a characteristic velocity scale, and T is a characteristic timescale. Injecting this scaling in Eq. (8), and since $(A_q - A_p)/(I_q + D_q) \sim 1/L^2$ for $\chi \gg 1$, one gets the characteristic angular velocity $\Omega \sim g^2T^3/L^2$. By using these estimates in Eqs. (6)–(9) and defining the dimensionless (starred) quantities as $U_p = UU_p^*$, $U_q = UU_q^*$, and $\Omega_r = \Omega^*\Omega_r$, we obtain

$$\frac{dU_p^*}{dt^*} - \epsilon\frac{\mathcal{A}}{\mathcal{B}}\Omega_r^*U_q^* = \mathcal{A}\cos\phi, \tag{10}$$

$$\frac{dU_q^*}{dt^*} + \epsilon\frac{\mathcal{B}}{\mathcal{A}}\Omega_r^*U_p^* = -\mathcal{B}\sin\phi, \tag{11}$$

$$\frac{d\Omega_r^*}{dt^*} = -\mathcal{C}U_p^*U_q^*, \tag{12}$$

$$\frac{d\phi}{dt^*} = \epsilon\Omega_r^*, \tag{13}$$

where $\mathcal{A} = (\bar{\rho} - 1)/(\bar{\rho} + A_p^*)$, $\mathcal{B} = (\bar{\rho} - 1)/(\bar{\rho} + A_q^*)$, $\mathcal{C} = (A_q^* - A_p^*)/(\bar{\rho}J_q^* + D_q^*)$, $A_p^* = A_p/(\rho V), A_q^* = A_q/(\rho V)$, $J_q^* = J_q/(\rho V L^2)$, and $D_q^* = D_q/(\rho V L^2)$, and $\epsilon = g^2T^4/L^2$ can be understood as the ratio of the characteristic timescale over a gravity timescale. In the following, we consider the small time limit $T \ll (L/g)^{1/2}$ or equivalently $\epsilon \ll 1$. We seek solutions of Eqs. (10)–(13) in the form of asymptotic expansions in powers of the small parameter $U_p^* = U_p^{*(0)} + \epsilon U_p^{*(1)} + \cdots$, $U_q^* = U_q^{*(0)} + \epsilon U_q^{*(1)} + \cdots$, $\Omega_r^* = \Omega_r^{*(0)} + \epsilon\Omega_r^{*(1)} + \cdots$, and $\phi = \phi^{(0)} + \epsilon\phi^{(1)} + \cdots$. The calculations are straightforward and are detailed in Appendix B. The solutions up to the order 1 with respect to the small parameter ϵ are

$$U_p^* = \mathcal{A}t^*\cos\phi^{(0)} - \frac{\epsilon}{12}\mathcal{A}^2\mathcal{B}\mathcal{C}t^{*5}\cos\phi^{(0)}\sin^2\phi^{(0)} + O(\epsilon^2), \tag{14}$$

$$U_q^* = -\mathcal{B}t^*\sin\phi^{(0)} - \frac{\epsilon}{12}\mathcal{A}\mathcal{B}^2\mathcal{C}t^{*5}\cos^2\phi^{(0)}\sin\phi^{(0)} + O(\epsilon^2), \tag{15}$$

$$\Omega_r^* = \frac{\mathcal{A}\mathcal{B}\mathcal{C}}{3}t^{*3}\cos\phi^{(0)}\sin\phi^{(0)} + O(\epsilon^2), \tag{16}$$

$$\phi = \phi^{(0)} + \epsilon\frac{\mathcal{A}\mathcal{B}\mathcal{C}}{12}t^{*4}\cos\phi^{(0)}\sin\phi^{(0)} + O(\epsilon^2). \tag{17}$$

Figure 2 displays the numerical and analytical solutions for a cylinder of aspect ratio 10 released with an orientation angle $\phi = 30^\circ$. We impose $\epsilon = 1$ such that $T = (L/g)^{1/2}$. The numerical solution is obtained by using a Runge-Kutta 4 algorithm. At $\bar{\rho} = 1.5$, the zeroth-order velocity component solutions exhibit good agreement with the numerical solution up to $t^* \approx 1.5$, while the first-order solutions maintain good agreement up to $t^* \approx 2.5$ [see Figs. 2(a) and 2(b)]. Additionally, the zeroth-order solution for the angular velocity demonstrates good agreement with the numerical solution up to $t^* = 3$. For moderately large density ratios, the agreement with the numerical solution is slightly worse [Figs. 2(d)–2(f)]. However, for the largest density ratios, the first-order analytical solutions remain valid up to $t^* \approx 5$ both for the first-order velocity component solutions and the angular velocity [Figs. 2(g)–2(i)]. It may appear surprising at first glance that agreement is much better for the zeroth-order angular velocity than for the zeroth-order velocity components. However, we recall that $\Omega_r^{*(1)} = 0$. Hence the zeroth-order solution for the angular velocity equals the first-order solution. For all the density ratios, we observe a good agreement between the analytical and numerical solutions out of the range of applicability of the analytical solution, which is $t^* \lesssim 1$. Moreover, this agreement depends on $\bar{\rho}$. The explanation lies in the magnitude of the coupling terms between translation and rotation in Eqs. (10) and (11). At first order these coupling terms are found to be proportional to $\mathcal{A}^2\mathcal{B}\mathcal{C}$ and $\mathcal{A}\mathcal{B}^2\mathcal{C}$ in Eqs. (14) and (15). Figure 3 illustrates the variation of $\mathcal{A}^2\mathcal{B}\mathcal{C}$ and $\mathcal{A}\mathcal{B}^2\mathcal{C}$ as a function of χ and $\bar{\rho}$. Both coupling terms have the same order of magnitude and are smaller than approximately 0.8. The behavior of $\mathcal{A}^2\mathcal{B}\mathcal{C}$ and $\mathcal{A}\mathcal{B}^2\mathcal{C}$ as a function of χ and $\bar{\rho}$ deserves also some comments. Since both quantities evolve comparably, we will focus on $\mathcal{A}^2\mathcal{B}\mathcal{C}$. This quantity increases as a function of χ for moderate χ. Hence one may expect a

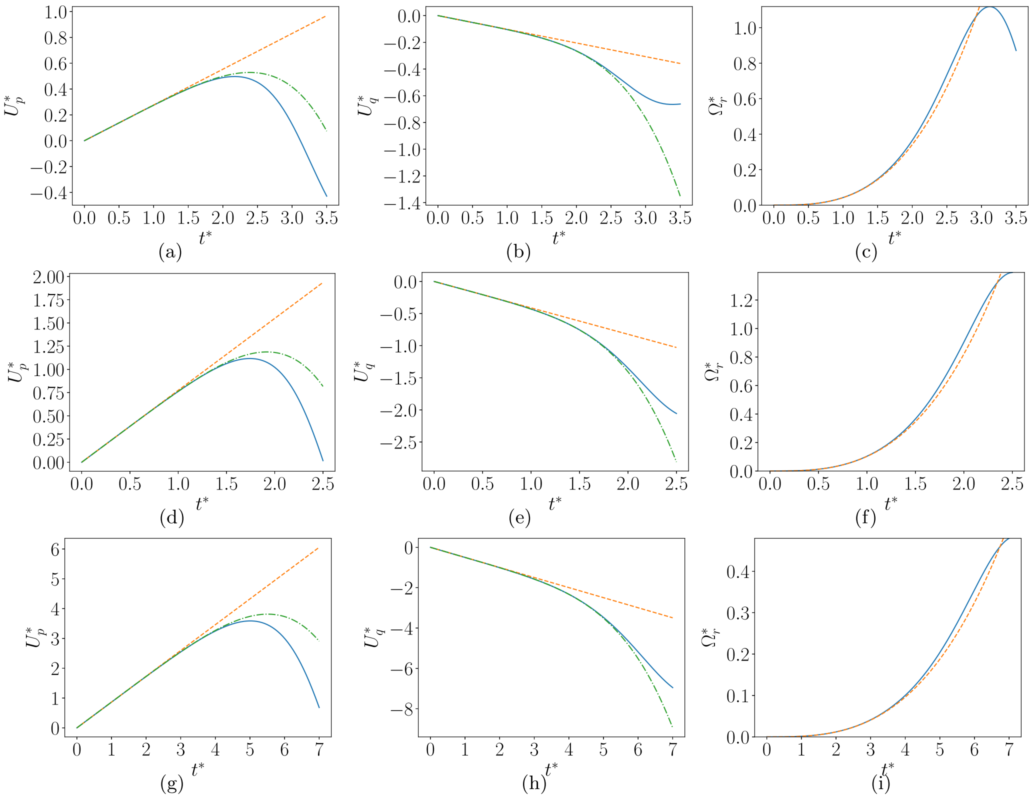

FIG. 2. Dimensionless velocities and angular velocity as function of time for a $\chi = 10$ cylinder starting from rest with $\phi = 30^\circ$ and $\epsilon = 1$. (a)–(c) $\bar{\rho} = 1.5$. (d)–(f) $\bar{\rho} = 10$. (g)–(i) $\bar{\rho} = 1000$. —, numerical solution of Eqs. (10)–(13); - -, zeroth-order asymptotic expansion; -·-, first-order asymptotic expansion.

better match of the theory for small cylinders. Then $\mathcal{A}^2\mathcal{B}\mathcal{C}$ becomes nearly independent of χ for $\chi \approx 20$. This weak dependence is in line with the results of Appendix A in which the added mass coefficients become almost independent of χ for this aspect ratio. $\mathcal{A}^2\mathcal{B}\mathcal{C}$ behaves nonmonotonously with $\bar{\rho}$. It increases for $\bar{\rho} \leqslant 5$ and then decreases for larger $\bar{\rho}$. The value of $\bar{\rho}$ for which we observed the maxima weakly depends on χ. All these trends can be easily obtained by looking more closely at the behavior of $\mathcal{A}^2\mathcal{B}\mathcal{C}$ as a function of $\bar{\rho}$. First one may note that for $\bar{\rho} \to 1$ we have

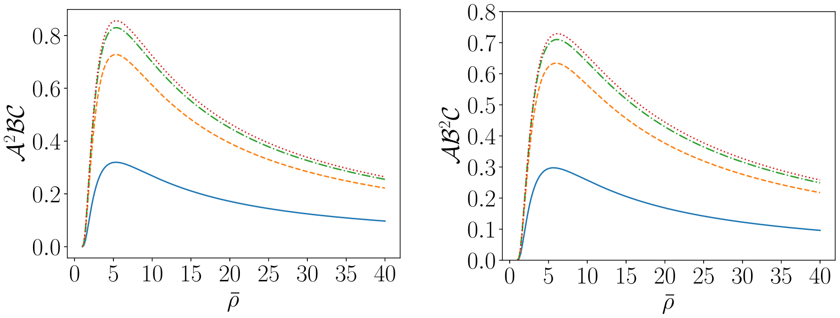

FIG. 3. Leading-order terms coupling translation and rotation. —, $\chi = 2$; - -, $\chi = 8$; -·-, $\chi = 32$; · · ·, $\chi \to \infty$.

$\mathcal{A}^2\mathcal{BC} \sim (\bar{\rho}-1)^3(A_q^*-A_p^*)/[(1+A_p^*)^2(1+A_q^*)(J_q^*+D_p^*)]$, which explains the strong increase of $\mathcal{A}^2\mathcal{BC}$ for $\bar{\rho} \leqslant 5$. In the opposite limit $\bar{\rho} \gg 1$ one obtains $\mathcal{A}^2\mathcal{BC} \sim 1/\bar{\rho} \times (A_q^*-A_p^*)/J_q^*$, which explains the decay of $\mathcal{A}^2\mathcal{BC}$ for a large density ratio.

It is also interesting to discuss the range of applicability of the asymptotic results in experiments. Our observations suggest that the asymptotic expansion is valid up to $t \sim (L/g)^{1/2}$ and an even larger value for large density ratios. Thus one may expect this solution to be valid as long as $(L/g)^{1/2} \ll D^2/\nu$, which can be written $\mathrm{Ar} \gg (\bar{\rho}-1)\chi$. This condition implies that the proposed analytical solution is expected to be observed in experiments for sufficiently inertial regimes. We are unaware of any experiments specifically dedicated to testing the validity of the theory. However, the qualitative observations provided in Toupoint *et al.* [25] may provide a first comparison with the present results. Toupoint *et al.* [25] investigated the settling of cylinder in the inertia-dominated regime $\mathrm{Ar} \approx 40\,000$. Their density ratio was fixed to $\bar{\rho} = 1.16$, and the elongation ratio of the cylinders ranged between 2 and 20. In particular, the time related to viscous diffusion in their experiments with a cylinder diameter 2 mm and $\chi = 5$ is $t_\nu \approx 4$ s, while $T \approx 0.03$ s. Hence the present theory should apply to their experimental results. They observed that the distance needed for the cylinders to rotate to their equilibrium position was less than $10d$ even when the cylinder was released vertically. From our analytical results, we obtain the time needed for the cylinder to change its orientation from nearly vertical ($\phi^{(0)} \ll 1$) to horizontal [$\phi(t^*) = \pi/2$], $t \sim (L/g)^{1/2}[6\pi/(\phi^{(0)}\mathcal{ABC})]^{1/4}$. With $\phi^{(0)} = \pi/10$ one obtains $t \approx 0.2$ s. Injecting this estimate in the velocity equation and integrating, one obtains the normalized distance l/D for which the cylinder changes its orientation: $l/D = \mathcal{A}gt^2/2 \approx 11.2$. This estimate is very close to the experimental prediction and gives confidence in the nonviscous flow origin on which this model is grounded.

IV. QUASISTEADY MODELS

The particle equations of motion (3)–(5) are coupled to the Navier-Stokes equations via the boundary conditions and the hydrodynamic loads. This makes the problem very hard to solve, and simplifying assumptions are required to make analytical progress, as explained in the Introduction. Since the characteristic time needed for the body to change its orientation scales like Ω^{-1}, the unsteady term in the Navier-Stokes equation scales as $\rho U\Omega$, where Ω and U may be taken as the nominal scales for the angular and settling velocities. Since the inertial term scales as $\rho U^2/L$, the unsteady term is negligible compared to the inertial term as long as $\Omega L/U \ll 1$. This condition is satisfied for a Reynolds number of unity when the time needed for the vorticity to diffuse from the body is much smaller than the rotation timescale [15]. In this limit, one may consider the fluid unsteady term and, as a consequence, the history loads to be negligible. To be entirely consistent with the neglect of the unsteady term, we will also neglect the added mass loads. It remains to consider the inertial correction to the loads proportional to ΩU. One may expect the ΩU corrections to be smaller than the inertial U^2 corrections as long as $\Omega L/U \ll 1$. Hence under this assumption, we postulate that both the history terms and the ΩU contribution are negligible with respect to the other load contribution as long as $\Omega L/U \ll 1$. The choice of the length of the particles ensures that the particle length is the relevant scale in the limit of a slender fiber [12,26]. The validity of the assumption $\Omega L/U \ll 1$ will be evaluated through comparisons with experimental results and direct numerical simulations in Sec. V.

A. Quasisteady models for an arbitrarily oriented cylinder

Under the assumption $\Omega L/U \ll 1$, the loads can be approximated as their quasisteady counterparts, disregarding the ΩU terms: $F_p^\omega \approx F_p$, $F_q^\omega \approx F_q$, and $-U_pU_q(A_q-A_p)+T_r^\omega \approx T_r^i + T_r^\Omega$, where F_p and F_q are the quasisteady forces in the longitudinal and perpendicular directions to the cylinder. The inertial torque, T_r^i, drives the cylinder towards its equilibrium position, while the hydrodynamic torque, T_r^Ω, resists rotation. We will distinguish two configurations depending on the cylinder aspect ratio: moderately long rods $2 \leqslant \chi \leqslant 30$ and long fibers $\chi > 30$. For $\chi \leqslant 30$, expressions derived through slender-body theory and direct numerical simulations by Kharrouba *et al.* [27], Pierson *et al.* [18], and Fintzi *et al.* [19] will be used, as they provide more accurate predictions compared to those by Khayat and Cox [12]. Conversely, the expression by Khayat and Cox [12] will be used for $\chi > 30$. To the author's knowledge, finite-inertia effects have not been considered for a slender body rotating in a fluid at rest at infinity. Thus, the most accurate expression for this case under the Stokes flow assumption by Pierson *et al.* [18] will be used. The expressions for F_p, F_q, T_r^i, and T_r^Ω are outlined in Appendix C. In both configurations, the linearized approximation is employed to describe the force as a function of the particle velocity. This approximation, which is exact in the Stokes flow regime, has been demonstrated to be accurate up to $\mathrm{Re} \approx 1$ for $10 \leqslant \chi \leqslant 30$ and up to $\mathrm{Re} \approx 10$ for $\chi < 10$ by Fintzi *et al.* [19], where $\mathrm{Re} = \rho D U/\mu$ is the Reynolds number based on the body diameter. The experimental works of Lopez and Guazzelli [28] with $11.5 \leqslant \chi \leqslant 34.5$ and Roy *et al.* [16] with $20 \leqslant \chi \leqslant 100$ have also validated its relevance for larger aspect ratios.

Equations (3)–(5) are normalized by defining dimensionless (starred) quantities as $U_p = UU_p^*$, $U_q = UU_q^*$, $\Omega_r = \Omega\Omega^*$, and $t = \Omega^{-1}t^*$, where the characteristic angular and velocity scales are *a priori* unknown. In the small inertia limit making use of the linearized approximation, the forces can be expressed as $F_p = -\mu U U_p^* L F_p^*(\mathrm{Re}_L^*, \chi)$ and $F_q = -\mu U U_q^* L F_q^*(\mathrm{Re}_L^*, \chi)$, where the expressions for F_p and F_q can be obtained from Appendix C. $\mathrm{Re}_L^* = \mathrm{Re}_L(U_p^{*2} + U_q^{*2})^{1/2}$ is the Reynolds number based on the instantaneous settling velocity, while $\mathrm{Re}_L = \rho U L/(2\mu)$ is the characteristic Reynolds number based on the body half-length. The inertial torque reads $-\rho U^2 U_p^* U_q^* L^3 T_i^*(\mathrm{Re}_L^*, \chi, \theta)$ while the torque resisting rotation reads $-\mu\Omega\Omega_r^* L^3 T_\Omega^*(\mathrm{Re}_\Omega^*, \chi)$, where $\mathrm{Re}_\Omega^* = \mathrm{Re}_\Omega|\Omega_r^*|$ and $\mathrm{Re}_\Omega = \rho\Omega D^2/\mu$. Injecting all those scalings in Eqs. (3)–(5), one obtains

$$\bar{\rho}\mathrm{Re}_\Omega\left(\frac{dU_p^*}{dt^*} - \Omega_r^* U_q^*\right) = -\frac{4}{\pi}F_p^*(\mathrm{Re}_L^*, \chi)U_p^* + \frac{(\rho_p - \rho)gD^2}{\mu U}\cos\phi, \tag{18}$$

$$\bar{\rho}\mathrm{Re}_\Omega\left(\frac{dU_q^*}{dt^*} + \Omega_r^* U_p^*\right) = -\frac{4}{\pi}F_q^*(\mathrm{Re}_L^*, \chi)U_q^* - \frac{(\rho_p - \rho)gD^2}{\mu U}\sin\phi, \tag{19}$$

$$\bar{\rho}\left(\frac{\mathrm{Re}_\Omega}{\mathrm{Re}}\right)^2 J_q^*\frac{d\Omega_r^*}{dt^*} = -\frac{4}{\pi}\left(T_i^*(\mathrm{Re}_L^*, \chi, \theta)U_p^* U_q^* + \frac{\mu\Omega}{\rho U^2}T_\Omega^*(\mathrm{Re}_\Omega^*, \chi)\Omega_r^*\right). \tag{20}$$

From the above set of equations and for moderate density ratios $\bar{\rho} \sim 1$, it appears that all the unsteady terms vanish if $\mathrm{Re}_\Omega \ll 1$ and $\mathrm{Re}_\Omega \ll \mathrm{Re}$. In contrast, we may consider the particle inertia [15] for large density ratios. We have to recall that to derive Eqs. (18)–(20), we have to assume $\Omega L/U \ll 1$, which is equivalent to $\mathrm{Re}_\Omega \ll \chi\mathrm{Re}$. This is a somewhat restrictive condition for the model applicability, but we shall see hereafter that it is valid for a non-negligible range of dimensionless parameters. Since the last terms in Eqs. (18)–(20) must be of order 1, the velocity and angular velocity scales can be readily obtained as $U \sim D^2(\rho_p - \rho)g/\mu$ and $\Omega = \rho D^4(\rho_p - \rho)^2 g^2/\mu^3$. Inserting these scalings yields

$$\bar{\rho}\mathrm{Ar}^2\left(\frac{dU_p^*}{dt^*} - \Omega_r^* U_q^*\right) = -\frac{4}{\pi}F_p^*(\mathrm{Re}_L^*, \chi)U_p^* + \cos\phi, \tag{21}$$

$$\bar{\rho}\mathrm{Ar}^2\left(\frac{dU_q^*}{dt^*} + \Omega_r^* U_p^*\right) = -\frac{4}{\pi}F_q^*(\mathrm{Re}_L^*, \chi)U_q^* - \sin\phi, \tag{22}$$

$$\bar{\rho}\mathrm{Ar}^2 J_q^*\frac{d\Omega_r^*}{dt^*} = -\frac{4}{\pi}(T_i^*(\mathrm{Re}_L^*, \chi, \theta)U_p^* U_q^* + T_\Omega^*(\mathrm{Re}_\Omega^*, \chi)\Omega_r^*). \tag{23}$$

The dimensionless nonlinear system of coupled differential equations, represented by Eqs. (21)–(23), describes the velocity and angular velocity of a cylinder under an external force. Analytical solutions to this system can only be obtained in the limit of low Archimedes number, as reported by Cox [5]. Otherwise, numerical solutions must be sought. The system exhibits two distinct regimes depending on St. For moderate particle inertia ($\mathrm{St} \sim 1$ or equivalently $\bar{\rho} \sim 1/\mathrm{Ar}^2$), as in the case of small solid particles settling in air, the left-hand sides (LHSs) of Eqs. (21)–(23) are non-negligible.

The resulting system consists of three ordinary differential equations, which are solved thanks to a Runge-Kutta 4 algorithm. Conversely, for small-particle inertia ($\mathrm{St} \ll 1$), as for small particles with densities close to that of the fluid, the LHS can be neglected. The simplified system is a nonlinear function composed of three equations, which can be solved using classical root-finding methods. It reads

$$0 = -\frac{4}{\pi} F_p^*(\mathrm{Re}_L^*, \chi) U_p^* + \cos\phi, \tag{24}$$

$$0 = -\frac{4}{\pi} F_q^*(\mathrm{Re}_L^*, \chi) U_q^* - \sin\phi, \tag{25}$$

$$0 = T_i^*(\mathrm{Re}_L^*, \chi, \theta) U_p^* U_q^* + T_\Omega^*(\mathrm{Re}_\Omega^*, \chi) \Omega_r^*. \tag{26}$$

The validity of the two sets of equations is restricted to the condition $\Omega L/U \ll 1$. Since $\Omega L/U \sim \mathrm{Ar}\chi$, we obtain the very restrictive condition $\mathrm{Ar} \ll 1/\chi$. The following section aims to demonstrate that the present set of equations remains valid up to moderate Archimedes numbers, despite its seemingly limited range of validity. It is also important to note that these scalings are *a priori* limited to small fluid inertial effects as the forces and resistive torque are viscous. However, Fintzi *et al.* [19] and Pierson *et al.* [18] have demonstrated that these viscous-based laws remain valid for moderate inertial effects ($\mathrm{Re}_L \leqslant 1$). The behavior for larger inertial effects is complex and nonlinearly dependent on the Reynolds number, as described in Appendix C.

B. Damped oscillations around $\phi = \pi/2$

Upon reaching its equilibrium position $\phi = \pi/2$, perpendicular to its direction of motion, an additional regime of interest can be expected for the particle. We linearize the equation of motion around this position. By writing $\phi(t) = \pi/2 + \epsilon\phi^*(t)$, where $\epsilon \ll 1$, the leading-order expressions for $\cos\phi$ and $\sin\phi$ are found to be $-\epsilon\phi^*$ and 1, respectively. For the velocity terms in the momentum equation to be nontrivial, they must scale as ϵU and U for the parallel and perpendicular velocity, respectively, such that $U_p = \epsilon U U_p^*$ and $U_q = U U_q^*$. By balancing the viscous torque with the inertial torque, we get $\Omega_r = \epsilon\Omega\Omega_r^*$ with $\Omega_r^* = d\phi^*/dt^*$, resulting in the following system of equations:

$$\mathrm{St}\left(\frac{dU_p^*}{dt^*} - \frac{d\phi^*}{dt^*} U_q^*\right) = -\frac{4}{\pi} F_p^*(\mathrm{Re}_L^*, \chi) U_p^* - \phi^*, \tag{27}$$

$$\mathrm{St}\left(\frac{dU_q^*}{dt^*} + \epsilon^2 \Omega_r^* U_p^*\right) = -\frac{4}{\pi} F_q^*(\mathrm{Re}_L^*, \chi) U_q^* - 1, \tag{28}$$

$$\mathrm{St} J_q^* \frac{d^2\phi^*}{dt^{*2}} = -\frac{4}{\pi}\left(T_i^*(\mathrm{Re}_L^*, \chi, \theta) U_p^* U_q^* + T_\Omega^*(\mathrm{Re}_\Omega^*, \chi) \frac{d\phi^*}{dt^*}\right). \tag{29}$$

Despite assuming a small angle around the equilibrium position, the resulting system comprises three coupled nonlinear equations, rendering analytical solutions for arbitrary Reynolds numbers impractical. However, various simplifications can be made. First, the second term on the left-hand side of Eq. (28) becomes negligible in the $\epsilon \ll 1$ limit. Second, using the velocity estimate mentioned above, $\mathrm{Re}_L^* \sim \mathrm{Re}_L |U_q^*|$ at leading order, resulting in Eq. (28) being decoupled from the other two equations. Third, in the long-time limit $t^* \gg \mathrm{St}$, the left-hand side of Eq. (28) becomes negligible, leading to $U_q^* \sim -\pi/4/F_q^*(\mathrm{Re}_L^*, \chi)$. Fourth, we consider the small inertia limit $\mathrm{Ar} \ll 1$. Under this limit, the system reads

$$\mathrm{St}\left(\frac{dU_p^*}{dt^*} + \frac{\pi}{4}\frac{1}{F_q^*}\frac{d\phi^*}{dt^*}\right) = -\frac{4}{\pi} F_p^* U_p^* - \phi^*, \tag{30}$$

$$\mathrm{St} J_q^* \frac{d^2\phi^*}{dt^{*2}} = \frac{T_i^*}{F_q^*} U_p^* - \frac{4}{\pi} T_\Omega^* \frac{d\phi^*}{dt^*}. \tag{31}$$

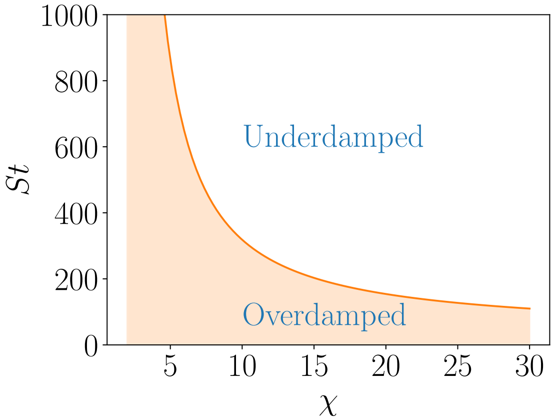

FIG. 4. Regime map showing the overdamped vs underdamped configuration in the (St, χ) plane. —, analytical criterion (33) for Ar $\ll 1$.

The resulting set of equations is made of two coupled linear ordinary differential equations (ODEs) since, in the limit Ar $\ll 1$, T_i^*, F_q^*, and T_Ω^* are independent of Re_L^*, Re_Ω^*, and θ. By substituting the expression for U_p from Eq. (31) into Eq. (30), the resulting equation becomes a third-order linear ODE with constant coefficients. Although an analytical solution may be obtained by summing three exponential functions, the coefficients inside these functions are complex and obey a third-order polynomial. Instead, we assume that the left-hand side of Eq. (30) is negligible compared to the right-hand side. This assumption is not satisfactory from a purely asymptotic perspective but allows for clearer disentanglement of the physical mechanism underlying the particle dynamic. In this limit, $U_p^* \approx -\pi/4/F_p^*(\mathrm{Re}_L^\chi)\phi^*$ and

$$\mathrm{St}J_q^*\frac{d^2\phi^*}{dt^{*2}} + \frac{4}{\pi}T_\Omega^*\frac{d\phi^*}{dt^*} + \frac{\pi}{4}\frac{T_i^*}{F_q^*F_p^*}\phi^* = 0. \tag{32}$$

The above equation is a classical damped harmonic oscillator. This equation shares many similarities with the one used by Gustavsson *et al.* [2,3], who investigated the effect of particle inertia on the orientation of spheroids in turbulent flows. Although the derivation presented in Gustavsson *et al.* [3] differs from the present one, they complement each other nicely. Two natural solutions exist depending on the sign of discriminant related to the second-order polynomial of this linear ODE. If the discriminant is positive, the solution is overdamped and leads to a motion decay without oscillation, while for a negative discriminant, the solution is underdamped and oscillatory motion is observed. Hence to obtain an underdamped solution, the particle must obey the following criteria:

$$\mathrm{St} > \frac{16}{\pi^3}\frac{T_\Omega^{*2}F_q^*F_p^*}{J_q^*T_i^*}, \tag{33}$$

which means that the particle inertia must be sufficiently large to lead to an oscillating regime. Under the condition Ar $\ll 1$, one may expect underdamped oscillation only when the density ratio is very high. Indeed, since the term on the right-hand side of (33) is of the order of 1, the Stokes number must be larger than a number of order 1. Considering that $\mathrm{St} = \bar{\rho}\mathrm{Ar}^2$, the density ratio $\bar{\rho}$ must be of the order of $1/\mathrm{Ar}^2$ to achieve an underdamped solution. In the case of low Archimedes numbers (Ar $\ll 1$), this implies $\bar{\rho} \gg 1$. Specifically, oscillatory motion can only be expected for high-density particles, such as steel, settling in the air for very low Archimedes numbers. Figure 4 presents a map of the two regimes. The critical Stokes number separating the two regimes is a decreasing function of χ. This assertion may be proved using scaling arguments for $\chi \gg 1$. Indeed under this assumption, $F_p^* \sim F_q^* \sim 1/\ln(\chi)$, $T_\Omega^* \sim 1/\ln(\chi)$, and $T_i^* \sim 1/\ln^2(\chi)$. Hence for $\chi \gg 1$

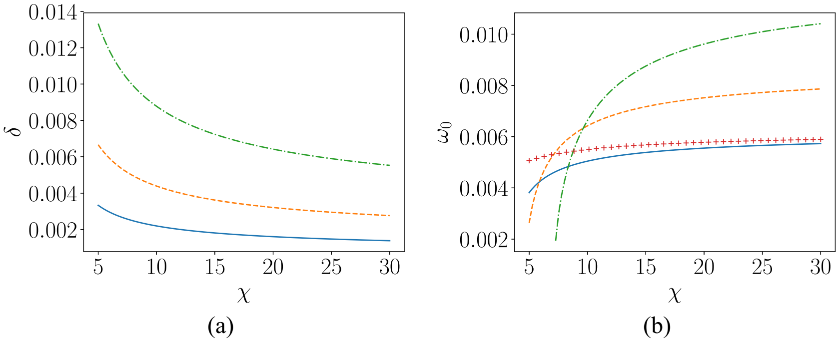

FIG. 5. (a) Evolution of δ [Eq. (34)] as a function of χ. (b) Evolution of ω_0 [Eq. (34)] as a function of χ. —, St = 2000; - -, St = 1000; -.-, St = 500; +, Eq. (35) for St = 2000.

the critical Stokes number decreases as $1/\ln^2(\chi)$. Hence, the underdamped regime will be promoted by using longer particles for a given Stokes number. If the criterion (33) is satisfied, the solution of Eq. (32) is given by

$$\phi^*(t) = Ae^{-\delta t^*}\cos(\zeta + \omega_0 t^*), \quad \text{where} \quad \delta = \frac{2}{\pi}\frac{1}{\mathrm{St}}\frac{T_\Omega^*}{J_q^*} \quad \text{and} \quad \omega_0 = \left(\frac{\pi}{4}\frac{1}{\mathrm{St}}\frac{T_i^*}{F_q^* F_p^* J_q^*} - \delta^2\right)^{1/2}. \tag{34}$$

A and ζ are constants given by the initial boundary conditions, while ω_0 is the dimensionless natural frequency of the oscillator and δ is the dimensionless damping coefficient. In the limit $\mathrm{St} \gg 1$, which is the relevant limit to expect underdamped oscillations, we obtain

$$\omega_0 = \left(\frac{\pi}{4}\frac{1}{\mathrm{St}}\frac{T_i^*}{F_q^* F_p^* J_q^*}\right)^{1/2}. \tag{35}$$

As the value of the Stokes number increases, both ω_0 and δ decrease, albeit with a less pronounced decrease observed for ω_0. Figure 5 displays the behavior of both quantities, which approach a near-constant value for $\chi \gg 1$. Specifically, as χ increases, $\delta \sim 1/(\mathrm{St}\ln\chi)$ while $\omega_0 \sim (1/\mathrm{St})^{1/2}$. The results for χ larger than 30 were not plotted; however, it is expected that the behavior for larger χ will remain consistent as all expressions for the loads converge to the slender body theory results for $\chi \gg 1$.

We may recall the many assumptions required to derive the model. In particular, we have assumed that the LHS of Eq. (30) is negligible. Upon substitution of our estimate for U_p, the LHS of Eq. (30) simplifies to $\pi/4\,\mathrm{St} d\phi^*/dt(1/F_q^* - 1/F_p^*)$. For $\chi \leqslant 10$, it has been reported that $F_q^* \approx F_p^*$ [19], leading to a near-cancellation of the LHS. However, for longer fiber, this assumption is debatable. Additionally, the model assumes that both the history loads and coupling effects between translation and rotation can be neglected. The former is questionable as the current model exhibits a constant period of oscillation while U_p is a decreasing function of time. Hence, in the long-time limit, the unsteady term in the Navier-Stokes equation may be much larger than the advective term. Therefore, the proposed model is not designed to provide an exact value for the damping coefficient and natural frequency for arbitrary dimensionless parameters, especially larger fluid inertia, but instead serves as a helpful framework for qualitatively understanding the origin of the damped oscillations observed in the subsequent section. Newsom and Bruce [15] investigated the settling of elongated graphite particles in air ($\bar{\rho} \approx 1442$, $\mathrm{Ar} \approx 0.054$, $\chi \geqslant 100$) and did not observe oscillations around their stable orientation. However, in their study, the Stokes number ($\mathrm{St} \approx 4.2$) is probably too low to expect such a phenomenon (see Fig. 4). The recent study of Bhowmick *et al.* [29] (not published

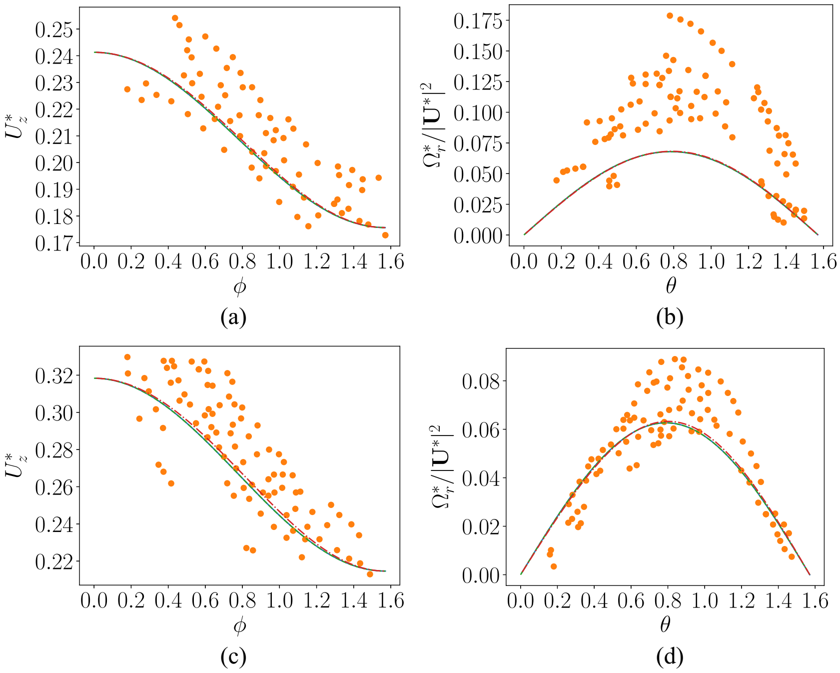

FIG. 6. Dimensionless sedimenting velocities. (a),(c) Dimensionless sedimenting velocity as a function of ϕ. (b),(d) Dimensionless angular velocity divided by the square of the particle velocity as function of θ (Fig. 1). ●, Cabrera *et al.* [20] experiments for $\mathrm{Ar} \approx 0.147$, $\bar{\rho} \approx 12.2$. —, prediction from the unsteady equations (21)–(23) for $\mathrm{Ar} \approx 0.147$; -·-, prediction from the unsteady equations (21)–(23) for $\mathrm{Ar} \approx 0.147$, $\bar{\rho} = 1000$; - -, prediction from the steady equations (24)–(26) for $\mathrm{Ar} \approx 0.147$. In the unsteady computations, we have not displayed the transient behavior of the particles starting from rest. The top panel corresponds to $\chi = 8$ and the bottom panel to $\chi = 16$.

yet), which focuses on the settling of an ellipsoidal particle with larger inertia in air, indicates that this solution is relevant.

V. COMPARISON OF THE QUASISTEADY MODELS WITH EXPERIMENTS AND DIRECT NUMERICAL SIMULATIONS

A. Experiments for Re ≪ 1

In this section, we compare the experimental results presented in Refs. [20] and [16] with those provided by the models presented in the previous section. Despite having previously compared our quasisteady results to those of Cabrera *et al.* [20] in Ref. [19], we present the comparison again as we aim to discuss the effect of the particle inertia further.

The sedimentation velocity and angular velocity measured in the study of Cabrera *et al.* [20] for particles with aspect ratios of $\chi = 8$ and 16 are presented in Figs. 6(a) and 6(c). For $\chi = 8$, the Reynolds number varies in the range $0.026 \leqslant \mathrm{Re} \leqslant 0.035$ and is slightly higher for $\chi = 16$ ($0.032 \leqslant \mathrm{Re} \leqslant 0.047$). The model predictions are consistent with the experimental data, with good agreement for the angular velocity for $\chi = 16$ but less so for $\chi = 8$ [Figs. 6(b) and 6(d)]. The experimental data for $\chi = 8$ exhibit considerable scatter, which the authors possibly attribute to particle defects, particularly mass inhomogeneities. The gravitational torque caused by mass inhomogeneities along the body axis, T_g, scales as $T_g \sim mgL$ [16]. The ratio of inertial torque to gravitational torque scales as $T_i/T_g \sim (\bar{\rho} - 1)\mathrm{Ar}\chi$. Therefore, for low Archimedes number and moderate aspect ratio, as in the present case, mass inhomogeneities may impact the angular

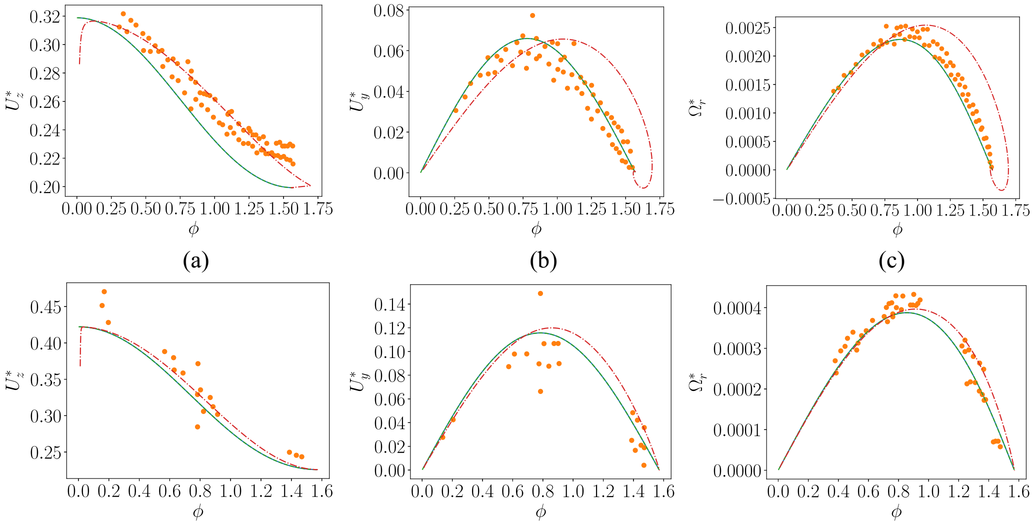

(a) (b) (c)

(d) (e) (f)

FIG. 7. Dimensionless sedimenting velocities. (a),(d) Vertical sedimenting velocity; (b),(e) drift velocity; and (c),(f) angular velocity. ●, Roy *et al.* [16] experiments for Ar ≈ 0.76 and $\bar{\rho} \approx 1.16$; —, prediction from Eqs. (21)–(23); – –, prediction from Eqs. (24)–(26); –·–, prediction from the unsteady equations (21)–(23) for Ar ≈ 0.76, $\bar{\rho} = 1000$. The top panel corresponds to $\chi \approx 20.5$ and the bottom panel to $\chi \approx 101$.

velocity. Additionally, the results obtained from both sets of equations, (21)–(23) and (24)–(26), are indistinguishable. Thus particle inertia can be safely neglected in the experiments of Cabrera *et al.* [20]. To further examine the impact of particle inertia, we conducted computations of the same physical configuration reported by Cabrera *et al.* [20] (with Ar ≈ 0.147 and $\chi = 8$ or 16), but with a significantly larger density ratio $\bar{\rho} = 1000$, which is representative of particles settling in air (represented by the dashed-dotted line in Fig. 6). Our results indicated that particle inertia has a minimal effect on the outcome. Indeed, the maximum value of Re_Ω^* was found to be approximately $\max(\mathrm{Re}_\Omega^*) \approx 9 \times 10^{-5}$, implying that the inertial term in the momentum equations, which scales as $\bar{\rho}\,\mathrm{Re}_\Omega$, remains much smaller than unity even with $\bar{\rho} = 1000$.

The sedimenting velocities and angular velocities as a function of ϕ, from the experiments of Roy *et al.* [16], are shown in Fig. 7. Although the angular velocity is not directly given in their work, it can be deduced from their plot of the inertial torque, as they utilize a quasisteady balance for angular momentum. The results obtained in this study match the experimental data except for Fig. 7(a). In this case, a non-negligible underestimation of the vertical velocity is observed when the cylinder is positioned perpendicular to the gravity vector. Furthermore, the difference between the sets of Eqs. (21)–(23) and (24)–(26) is once again negligible, indicating that particle inertia is negligible in the experiments of Roy *et al.* [16]. However, when considering more inertial particles ($\bar{\rho} = 1000$), deviations from the experimental data are observed. Specifically, the dimensionless velocities remain mostly unchanged in amplitude, but a noticeable shift to larger ϕ is observed. The system of ODEs represented by Eqs. (21)–(23) can be visualized as a phase portrait, as shown in Figs. 7(c) and 7(f). The stable fixed point located at $\phi = \pi/2$ is identified as a focus or spiral.

The oscillatory behavior of the angle as a function of time is evidenced in Fig. 8 for $\chi \approx 20.5$. Exponential decay of ϕ over time is observable for both the simplified model, expressed in Eq. (34), and the complete numerical solution. However, we may observe discrepancies between the two models both for the slope and oscillation period. This is not surprising due to the many assumptions required to derive the model. The analytical solution only offers a qualitative depiction of the underdamped behavior in this inertial configuration.

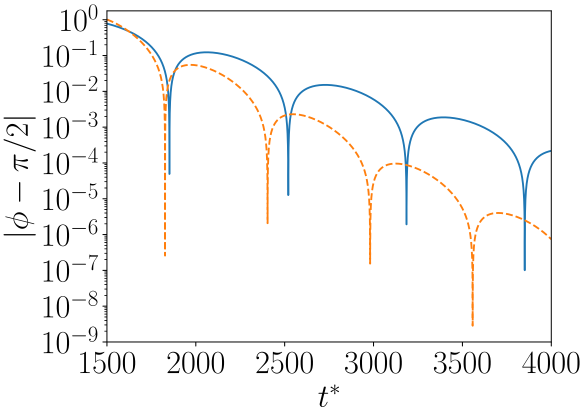

FIG. 8. Evolution of $|\phi - \pi/2|$ as a function of time with $\mathrm{Ar} \approx 0.76$, $\bar{\rho} = 1000$, and $\chi \approx 20.5$. —, prediction from Eqs. (21)–(23); - -, prediction from Eq. (34) with $\mathrm{Re} \approx 0.156$ and $\mathrm{Re}_\Omega \ll 1$.

B. Direct numerical simulations for Re ∼ 1

In the preceding subsection, we have demonstrated the unexpected agreement of the quasisteady equations with various literature findings for $\mathrm{Re} \ll 1$. However, no experiments of such nature have been conducted for higher Reynolds numbers, and to the best of our knowledge there are no available simulations. Therefore, we conducted direct numerical simulations to validate the applicability of the model at higher Reynolds numbers ($\mathrm{Re} \sim 1$).

1. Numerical methodology

Computations are carried out with the PELIGRIFF code [30]. This code was used to investigate the settling of spherical and angular particles [31,32]. In brief, the code solves the three-dimensional Navier-Stokes equations using a finite-volume discretization on a staggered grid. The time-stepping strategy for the fluid phase is done thanks to second-order time-accurate Crank-Nicolson and Adams-Bashforth schemes. To enforce the rigid-body motion inside the solid region, a Lagrange multiplier/fictitious domain (DLM/FD) is used. We use a uniform distribution of the Lagrangian points along the surface of the cylindrical body as detailed in [33]. More details on the numerical methods can be found in Ref. [30]. We explore the effect of χ, Ar, and $\bar{\rho}$ within the range $\chi = \{2, 4\}$, $\mathrm{Ar} = \{24, 96\}$, and $\bar{\rho} = \{1.5, 10\}$. The cylinder is initiated with an angle $\phi = 5^\circ$, and it is released at rest. In addition, a case with a larger density ratio was computed with a starting angle of $\phi = 60^\circ$ to investigate the damped oscillation regime specifically. The computational domain for this problem is depicted in Fig. 9. Its characteristic size length depends on the aspect ratio: for $\chi = 2$, $\mathcal{L} = 12D$ while for $\chi = 4$, $\mathcal{L} = 15D$. Note that the value prescribed for $\chi = 2$ is larger than that used in [32]. We have checked that the present domain was sufficiently large by increasing its size of 25% in all directions finding less than 2% error on $\Omega L/U$ for the more challenging configuration ($\mathrm{Ar} = 24$, $\chi = 4$). Obviously, larger domains might be used to avoid this small effect of the boundaries at the expense of a substantially larger numerical cost. However, we have to recall that the present paper is not aimed to provide domain size perfectly independent simulations of the problem but rather to provide a bound to the quasisteady assumptions. To this aim, we compare the numerical results to the model of Sec. IV, which relies heavily on fit and contains some minor errors concerning the simulation from which they are extracted. Regarding the boundary conditions, the domain is biperiodic in the lateral directions, while zero velocity and outflow conditions are imposed on the upstream and downstream boundaries, respectively. A uniform cell distribution is imposed in a rectangular region depicted in Fig. 9 as an orange volume. This region is located $2D$ below the middle of the domain and extends up to $6D$ in the direction of gravity. In this flow region, 25 cells

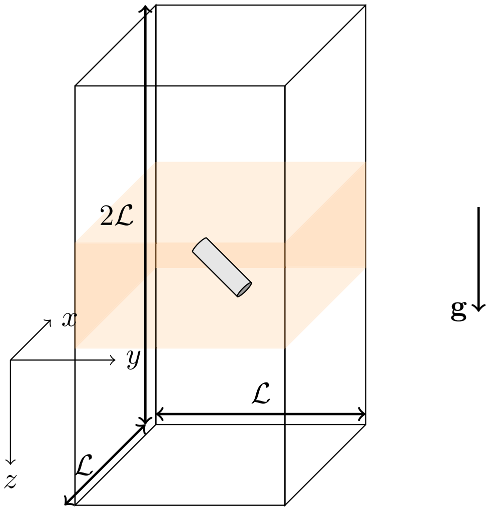

FIG. 9. Scheme of the computational domain (not to scale).

are distributed per body diameter, which is sufficient to accurately compute the particle dynamic for the range of Reynolds number investigated [33]. The number of cells per mesh is 26 million for $\chi = 2$ and 46 million for $\chi = 4$. The time step is imposed such that the CFL always fall below 0.25. To prevent the cylinder from exiting the numerical domain, the computational domain is moved vertically to keep the particle at least at a distance of $10D$ of the upstream boundary. More details on the domain translation technique can be found in Refs. [31,32]. The magnitude of this domain translation is chosen to be the grid size ($D/25$). The simulations are run up until the cylindrical particle reaches its equilibrium position.

2. *Numerical results*

To investigate the impact of moderate inertia on the rod motion, we first consider the situation $\mathrm{Ar} = 24$. In this scenario, the Reynolds number will fluctuate between 1.7 and 1.9 when χ equals 2, and between 2 and 2.7 when χ is 4.

For the shortest cylinder with aspect ratio $\chi = 2$, there is a noticeable agreement between the results obtained from Eqs. (21)–(23) (including particle inertia) and those from direct numerical simulations, as illustrated in Figs. 10(a)–10(c). However, the agreement is better for U_y^* than for the other quantities. In practice, ascertaining the precise origin of the slight discrepancy for the remaining quantities proves to be challenging. The most plausible explanation lies in the semiempirical nature of the formulas for the quasisteady loads presented in Appendix C. These formulations were derived through numerical fitting of direct numerical simulation results. Despite rigorous validation of the direct simulations, minor errors may inadvertently arise during the fitting process, depending on the specific load considered, potentially influencing the results. Varying the density ratio from 1.5 to 10 has a negligible effect on the sedimentation velocities in this case. In Figs. 10(d)–10(f), we present the results for $\chi = 4$. Although there is a qualitative agreement between the model and the numerical results, the model overestimates the drift and angular velocities. Moreover, for $\chi = 4$, the effect of particle inertia on the sedimentation velocities is more pronounced. In particular, this case exhibits underdamped motion. To investigate this oscillating behavior further, we have carried out one simulation of the settling of a rod with the same dimensionless parameters ($\mathrm{Ar} = 24$, $\chi = 4$) but with a much larger density ratio ($\bar{\rho} = 50$). To maintain reasonable computational time, the simulation is initiated with $\phi = 60^\circ$. There is a good agreement between the simulation and the model, even if the model overpredicts the angular velocity (Fig. 11). We recall that we neglect the

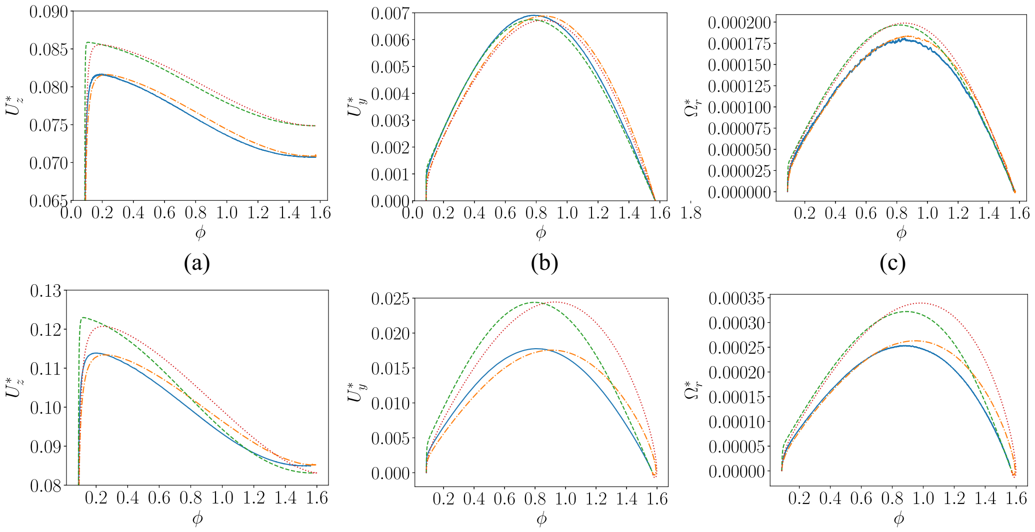

(a) (b) (c)

(d) (e) (f)

FIG. 10. Dimensionless sedimenting velocities for Ar = 24. (a),(d) vertical sedimenting velocity; (b),(e) drift velocity; and (c),(f) angular velocity. ——, direct numerical simulation results with $\bar{\rho} = 1.5$; -·-, direct numerical simulation results with $\bar{\rho} = 10$; - -, prediction from Eqs. (21)–(23) with $\bar{\rho} = 1.5$; . . ., prediction from Eqs. (21)–(23) with $\bar{\rho} = 10$. The top panel corresponds to $\chi = 2$ and the bottom panel to $\chi = 4$.

history loads in Eqs. (21)–(23), which may affect the initial transient since the rod starts from rest. One may also observe a good agreement between the oscillating period, the decrease in amplitude given by the numerical results, and the model made of Eqs. (21)–(23) [Fig. 11(b)]. This is somehow surprising since there is *a priori* no reason for neglecting the history loads in the underdamped regime. They appear to have a negligible effect on this regime.

We now consider much more significant inertia effects (Ar = 96). Within this regime, the Reynolds number is found to vary between 5.3 and 6.2 for $\chi = 2$ and between 5.8 and 8.6 for $\chi = 4$. Surprisingly, the quasisteady model exhibits good agreement with numerical results for $\chi = 2$ [as depicted in Figs. 12(a)–12(c)], despite the significant role played by inertia effects. However, for $\chi = 4$, the model overestimates both the drift velocity and angular velocity [as shown in Figs. 12(d)–12(f)]. We observe that all configurations result in underdamped regimes.

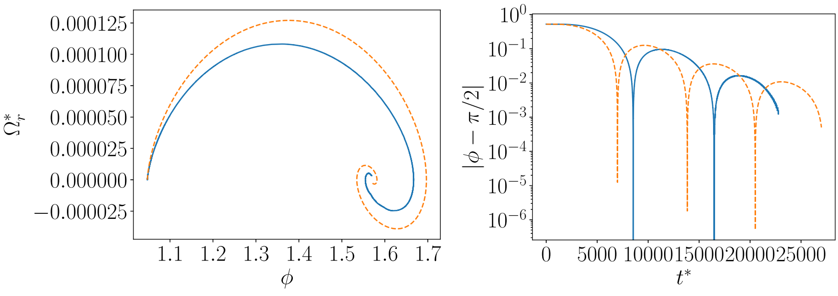

(a) (b)

FIG. 11. Comparison between the simulation results and the quasisteady model with Ar = 24, $\chi = 4$, and $\bar{\rho} = 50$. (a) Phase space diagram of the oscillator. (b) Time evolution of the inclination angle. ——, direct numerical simulation results; - -, prediction from Eqs. (21)–(23).

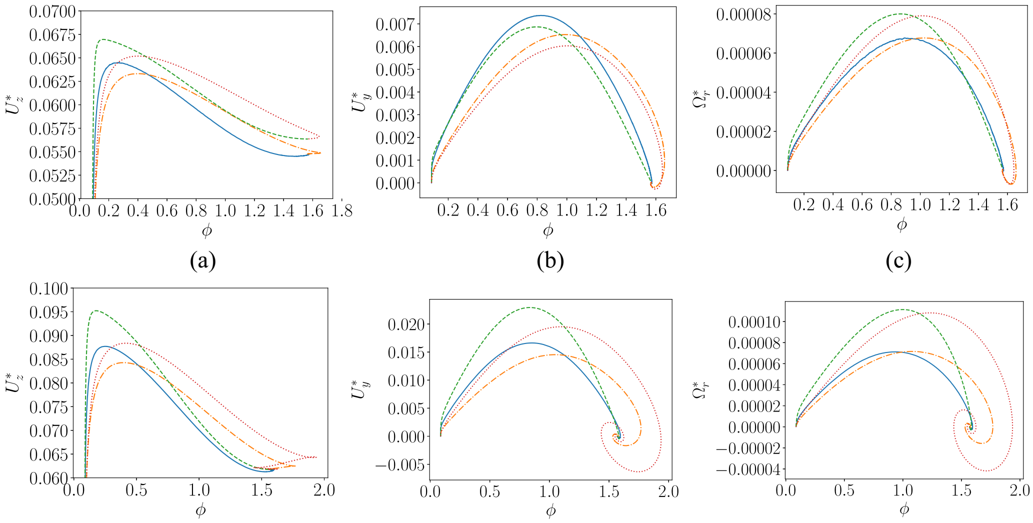

(a) (b) (c)

(d) (e) (f)

FIG. 12. Dimensionless sedimenting velocities for Ar = 96. (a),(d) Vertical sedimenting velocity; (b),(e) drift velocity; and (c),(f) angular velocity. ——, Direct numerical simulation results with $\bar{\rho} = 1.5$; – · –, direct numerical simulation results with $\bar{\rho} = 10$; – –, prediction from Eqs. (21)–(23) with $\bar{\rho} = 1.5$, . . ., prediction from Eqs. (21)–(23) with $\bar{\rho} = 10$. The top panel corresponds to $\chi = 2$ and the bottom panel to $\chi = 4$.

This regime is much more pronounced for $\chi = 4$ and $\bar{\rho} = 10$ than for $\chi = 2$ and $\bar{\rho} = 1.5$, for which the amplitude of oscillation is small and nearly indistinguishable. Finally, we compare the numerical and model-based results [derived from Eqs. (21)–(23)] for Ar = 96, $\chi = 4$, and $\bar{\rho} = 10$ by examining the oscillation period and the decay of amplitude. The results are displayed in Fig. 13. The model slightly underpredicts the amplitude decay as well as the oscillation period.

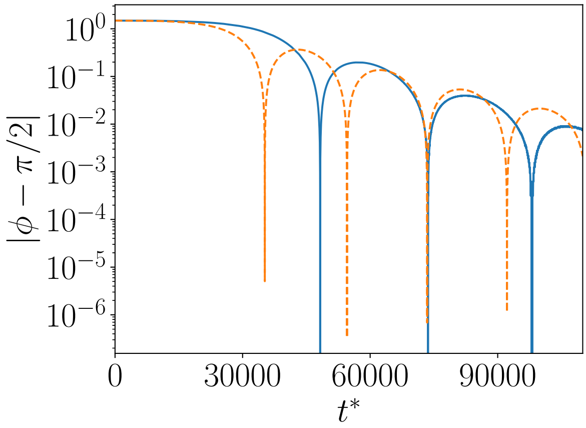

FIG. 13. Time evolution of the inclination angle (Ar = 96, $\chi = 4$, $\bar{\rho} = 10$). ——, Direct numerical simulation results; – –, prediction from Eqs. (21)–(23).

TABLE I. Values of $\max(\Omega_r L/|\mathbf{U}|)$ in the experiments of [16,20] and in the simulation results.

	Cabrera *et al.* [20]		Roy *et al.* [16]		Direct numerical simulations			
	$\mathrm{Ar} \approx 0.147$		$\mathrm{Ar} \approx 0.76$		$\mathrm{Ar} = 24$		$\mathrm{Ar} = 96$	
	$\chi = 8$	$\chi = 16$	$\chi = 20$	$\chi = 100$	$\chi = 2$	$\chi = 4$	$\chi = 2$	$\chi = 4$
$\max(\Omega_r L/|\mathbf{U}|)$	0.024	0.035	0.12	0.11	0.13	0.25	0.2	0.33

VI. DISCUSSION AND CONCLUSION

Based on the results presented above, two main conclusions can be drawn. First, it can be inferred that the quasisteady assumption holds across a broad range of dimensionless parameters, as it is supported by both the experiments conducted by Cabrera *et al.* [20] and Roy *et al.* [16] and by the direct numerical simulations. Although these experiments and simulations do not strictly obey the condition $\mathrm{Ar} \ll 1/\chi$, the quasisteady assumption is still valid for a significantly more extensive range of values than initially predicted. This can be attributed to the magnitude of the angular velocity Ω, which has the correct scaling but is at least three orders of magnitude smaller than the anticipated value. This feature arises from the specific values of dimensionless steady loads, namely F_p^*, F_q^* T_i^*, and T_Ω^*. Indeed, let us consider the case $\chi \gg 1$ and $\mathrm{Ar} \ll 1$. Under these limits, we have $F_p^* = 2\pi/\ln\chi$, $F_q^* = 4\pi/\ln\chi$, $T_i^* = 5\pi/(24\ln^2\chi)$, and $T_\Omega^* = \pi/(3\ln\chi)$ [4,12]. By employing Eqs. (24) and (25), we can deduce $U_p^* = \cos\phi\ln\chi/8$ and $U_q^* = -\sin\phi\ln\chi/16$. Substituting these estimates into Eq. (26), we finally obtain $\Omega_r^* = 5\sin(2\phi)\ln\chi/2048$. Consequently, for $\chi = 10$, the maximum value of Ω_r^* is $\max(\Omega_r^*) \approx 0.0056$, which offers a reasonable explanation for the observed values of the angular velocity. As a result, $\Omega L/U \ll 1$ for all configurations except the highest inertial simulations (see Table I). Additionally, these findings support the notion that the quasisteady assumption remains valid as long as $\Omega L/U \ll 1$, thereby strengthening our analysis.

Second, it can be concluded, based on the results of the previous section, that particle inertia plays no significant role in the magnitude of the sedimenting velocities in the system under investigation. Hence, a correct estimate of $\Omega L/U$ can be obtained by disregarding the particle inertia in the equations of motion and considering the system made of Eqs. (24)–(26). We have solved this system for $\chi \in [2; 500]$ and $\mathrm{Ar} \in [0.001; 150]$ by using the semiempirical expression for the loads proposed by Fintzi *et al.* [19] for $\chi \leqslant 30$ and Khayat and Cox [12] theory for $\chi > 30$. In each of the runs, we have computed the maximum value of $\Omega_r L/|\mathbf{U}|$ (Fig. 14).

For $\mathrm{Ar}\chi \leqslant 10$ except for the smallest aspect ratio, $\Omega L/U$ scales as $\mathrm{Ar}\chi$, in agreement with our scaling analysis. For larger $\chi\mathrm{Ar}$ the rate of increase of $\Omega L/U$ decreases strongly, especially

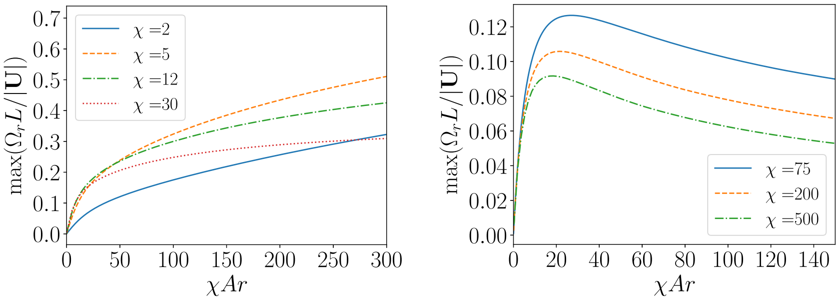

(a) (b)

FIG. 14. Evolution of $\max(\Omega_r L/|\mathbf{U}|)$ with $\chi\mathrm{Ar}$. Equations (24)–(26) are solved using a root-finding algorithm for 20 values of ϕ ranging between 0 and $\pi/2$.

for $\chi \geqslant 12$. Indeed, qualitatively different behavior may be observed for moderate inertial effects ($\mathrm{Re}_L \sim 1$) and very large aspect ratios ($\chi \gg 1$). Fintzi *et al.* [19] observed that for $\chi = 30$, the inertial torque scales as $T_i/(\mu U L^2) \sim \mathrm{Re}_L^{1/3}$, yielding $T_i \sim \rho^{1/3}\mu^{2/3}U^{4/3}L^{7/3}$. By balancing this inertial torque with the resistive torque, we obtain $\Omega \sim \rho^{1/3}\mu^{-1/3}U^{4/3}L^{-2/3}$ and $\Omega L/U \sim \mathrm{Re}_L^{1/3}$. Using the same scaling as in Sec. IV for the velocity, we obtain $\Omega L/U \sim \mathrm{Ar}^{1/3}\chi^{1/3}$. Therefore, the rate of increase of $\Omega L/U$ is slower as the Reynolds number increases for elongated particles. This trend is even more pronounced for very long fibers [Fig. 14(b)]. In this regime, Khayat and Cox [12] demonstrated that the inertial torque decreases with the Reynolds number for $\mathrm{Re}_L \geqslant 4$. However, the validity of their theory for such high Reynolds numbers may be questionable, as their asymptotic solution requires $\mathrm{Re}_L \ll \ln(\chi)$. Nonetheless, simulations performed by Khair and Chisholm [34] and Shin *et al.* [17] indicate that the solutions proposed by Khayat and Cox [12] remain valid for $\mathrm{Re}_L \approx 10$ and $\mathrm{Re}_L \approx 5$, respectively, for the longitudinal force on a long spheroid aligned with the flow direction and the torque on a long fiber, with $\chi = 100$. Moreover, the models of Khayat and Cox [12] are in very good agreement with the experimental results of Roy *et al.* [16] for $\chi = 100$ and $\mathrm{Re}_L \approx 7.6$. Consequently, the solution provided by Khayat and Cox [12] is considered to provide quantitatively accurate results up to $\mathrm{Re}_L \approx 10$ as long as the fiber is adequately elongated ($\chi \geqslant 100$). If we consider that the quasisteady assumption fails for values of $\Omega L/U$ larger than 0.2, then we can expect the quasisteady models to be accurate for $\chi\mathrm{Ar} \approx 200$ if $\chi = 2$, and for $\chi\mathrm{Ar} \approx 40$ if $2 < \chi \leqslant 30$. However, the quasisteady assumption should remain valid for more elongated fibers as long as the underlying assumptions made in the derivation of the models of Khayat and Cox [12] are fulfilled, particularly if $\mathrm{Re} \ll 1$.

This paper also focuses on the underdamped regime and its characteristics, such as oscillation period and amplitude decrease rate. It was found that the most simple model, i.e., the underdamped oscillator, qualitatively reproduces numerical results but not quantitatively. This may have significant implications for atmospheric flows where particle orientation is driven by this solution [2,3]. To improve the model, particle inertia could be included in the parallel velocity equation, resulting in a third-order linear ordinary differential equation that can be easily solved. A natural perspective to this model might be to study the oscillatory motion of a rod settling under gravity, such as a fluttering motion [25]. However, in such high inertial flow, there is no reason for the quasisteady assumption to remain valid [35]. Moreover, even under the quasisteady limit, the loads on such bodies at high Reynolds numbers are only known for very few configurations [27,33].

ACKNOWLEDGMENTS

ANR MUSCATs financial support is greatly appreciated. We thank Bernhard Mehlig for stimulating discussions and for pointing out the former studies on the underdamped oscillator. The author is indebted to Greg Voth for providing the experimental data of Roy *et al.* [16]. We also thank Jacques Magnaudet for fruitful discussions on the added mass torque. We used CHATGPT and Grammarly to improve the quality of the written text.

APPENDIX A: ADDED MASS COEFFICIENTS

In this Appendix, we compute the coefficient A_p, A_q, and D_q by using the JADIM code for $1 \leqslant \chi \leqslant 15$. The numerical details concerning the code as well as the mesh properties can be found elsewhere [18,22,27]. At the time $t = 0$, we impose a constant linear or angular acceleration to a cylinder initially at rest. Since in the very short time limit viscous and rotational contributions are negligible in comparison to potential flow contribution [21], one can easily recover the added mass coefficients by computing the loads on the body. Figure 15 displays the dimensionless added mass coefficient $A_p^* = A_p/(\rho V)$, $A_q^* = A_q/(\rho V)$, and $D_q^* = D_q/(\rho V L^2)$ as a function of the aspect ratio. A good agreement is observed between the present results and those of Loewenberg [9] obtained using potential flow calculations. In the limit $\chi \gg 1$, χA_p^* and A_q^* tend toward a constant value. For

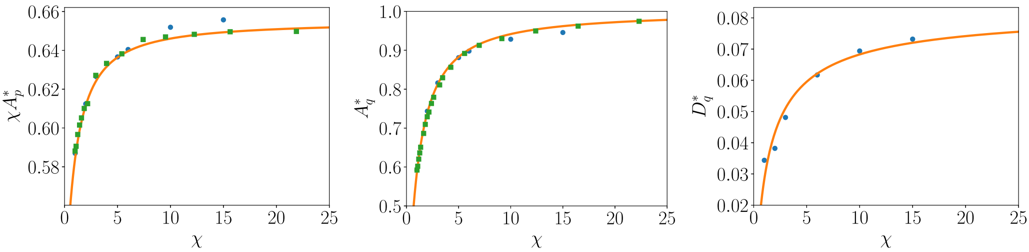

FIG. 15. Dimensionless added mass coefficients as a function of χ. 🟩, Loewenberg [9] results; ●, present results based on JADIM code [22]; —, fits.

the particular case A_q^* this constant is simply 1, i.e., the added mass coefficient on an infinitely long cylinder perpendicular to the flow direction. As a result, we propose the following correlation:

$$A_p^* = \frac{1}{\chi}\left(0.655 - \frac{0.141}{1+\chi^{1.17}}\right), \tag{A1}$$

$$A_q^* = 1 - \frac{0.828}{1+\chi^{1.12}}. \tag{A2}$$

To the best of our knowledge, the functional dependency of D_q^* with respect to χ has not been published yet in the literature, at least for $\chi \geqslant 1$. Figure 15 shows that in the limit $\chi \gg 1$, D_q^* tends toward a constant value which is *a priori* unknown. However, in the case of a Rankine ovoid, for $\chi \gg 1$, $D_q^* \approx 1/12$ [23]. Since in the limit of a large aspect ratio one may assume that the rounded ends of the Rankine ovoid have little effect on the added mass coefficient, we propose the following empirical correlation:

$$D_q^* = \frac{1}{12} - \frac{0.11}{(1+\chi^{0.8})}, \tag{A3}$$

which matches closely the numerical results.

APPENDIX B: SHORT-TIME ASYMPTOTIC EXPANSION

We calculate the leading-order terms of the short-time asymptotic expansion. Since $\cos(\phi^{(0)} + \epsilon\phi^{(1)}) \sim \cos\phi^{(0)} - \epsilon\phi^{(1)}\sin\phi^{(0)}$ and $\sin(\phi^{(0)} + \epsilon\phi^{(1)}) \sim \sin\phi^{(0)} + \epsilon\phi^{(1)}\cos\phi^{(0)}$ at zeroth order, Eqs. (10)–(13) simplify to

$$\frac{dU_p^{*(0)}}{dt^*} = \mathcal{A}\cos\phi^{(0)}, \tag{B1}$$

$$\frac{dU_q^{*(0)}}{dt^*} = -\mathcal{B}\sin\phi^{(0)}, \tag{B2}$$

$$\frac{d\Omega_r^{*(0)}}{dt^*} = -\mathcal{C}U_p^{*(0)}U_q^{*(0)}, \tag{B3}$$

$$\frac{d\phi^{(0)}}{dt^*} = 0. \tag{B4}$$

The zeroth-order solution is easily obtained and reads

$$U_p^{*(0)} = \mathcal{A}t^*\cos\phi^{(0)}, \tag{B5}$$

$$U_q^{*(0)} = -\mathcal{B}t^*\sin\phi^{(0)}, \tag{B6}$$

$$\Omega_r^{*(0)} = \frac{\mathcal{ABC}}{3} t^{*3} \cos\phi^{(0)} \sin\phi^{(0)}, \tag{B7}$$

$$\phi^{(0)} = \phi(t^* = 0), \tag{B8}$$

where we have assumed that the cylinder starts from rest. At first order, Eqs. (10)–(13) give

$$\frac{dU_p^{*(1)}}{dt^*} = \frac{\mathcal{A}}{\mathcal{B}} \Omega_r^{*(0)} U_q^{*(0)} - \mathcal{A}\phi^{(1)} \sin\phi^{(0)}, \tag{B9}$$

$$\frac{dU_q^{*(1)}}{dt^*} = -\frac{\mathcal{B}}{\mathcal{A}} \Omega_r^{*(0)} U_p^{*(0)} - \mathcal{B}\phi^{(1)} \cos\phi^{(0)}, \tag{B10}$$

$$\frac{d\Omega_r^{*(1)}}{dt^*} = 0, \tag{B11}$$

$$\frac{d\phi^{(1)}}{dt^*} = \Omega_r^{*(0)}, \tag{B12}$$

which leads to

$$U_p^{*(1)} = -\frac{1}{12} \mathcal{A}^2 \mathcal{BC} t^{*5} \cos\phi^{(0)} \sin^2\phi^{(0)}, \tag{B13}$$

$$U_q^{*(1)} = -\frac{1}{12} \mathcal{AB}^2 \mathcal{C} t^{*5} \cos^2\phi^{(0)} \sin\phi^{(0)}, \tag{B14}$$

$$\Omega_r^{*(1)} = 0, \tag{B15}$$

$$\phi^{(1)} = \frac{\mathcal{ABC}}{12} t^{*4} \cos\phi^{(0)} \sin\phi^{(0)}. \tag{B16}$$

APPENDIX C: QUASISTEADY LOADS

The expression of the quasisteady loads used in this paper can be found below.

1. Moderately long rods: $\chi \leqslant 30$

a. Expression of F_p

The expression of F_p reads [19]

$$F_p(\mathrm{Re}_L^*, \chi, \theta) = -2\pi\mu|\mathbf{U}|L\cos\theta \left(\frac{A^{(1)}_{\mathrm{Re}=0} + A^{(1)}(\mathrm{Re}_L^*)}{\ln(2\chi)} + \frac{A^{(2)}_{\mathrm{Re}=0} + A^{(2)}(\mathrm{Re}_L^*)}{\ln^2(2\chi)} + \frac{A^{(3)}_{\mathrm{Re}=0} + A^{(3)}(\mathrm{Re}_L^*)}{\ln^3(2\chi)} \right.$$
$$\left. + \frac{A^{(4)}_{\mathrm{Re}=0} + A^{(4)}(\mathrm{Re}_L^*)}{\ln^4(2\chi)} + \frac{2.34}{\chi^{2/3}\left(\chi - \frac{1}{2}\right)^{1.75}} \right), \tag{C1}$$

where $A^{(1)}_{\mathrm{Re}=0} = 1$, $A^{(2)}_{\mathrm{Re}=0} \approx 0.807$, $A^{(3)}_{\mathrm{Re}=0} \approx 0.829$, $A^{(4)}_{\mathrm{Re}=0} \approx 1.45$ [27]. The first-order inertial correction is null, $A^{(1)}(\mathrm{Re}_L^*) = 0$, while the second-, third-, and fourth-order inertial functions read

$$A^{(2)}(\mathrm{Re}_L^*) = \frac{1}{2}\left(\frac{E_1(2\,\mathrm{Re}_L^*) + \ln(2\,\mathrm{Re}_L^*) - e^{-2\,\mathrm{Re}_L^*} + \gamma + 1}{2\,\mathrm{Re}_L^*} + E_1(2\,\mathrm{Re}_L^*) + \ln(2\,\mathrm{Re}_L^*) + \gamma - 2 \right), \tag{C2}$$

$$A^{(3)}(\mathrm{Re}_L^*) = A_A^{(3)}(\mathrm{Re}_L^*) + A_B^{(3)}(\mathrm{Re}_L^*) + 2A^{(2)}(\mathrm{Re}_L^*)\ln(2), \tag{C3}$$

$$A^{(4)}(\mathrm{Re}_L^*) = 3\ln(2)\left(A_A^{(3)}(\mathrm{Re}_L^*) + A_B^{(3)}(\mathrm{Re}_L^*)\right) + 3A^{(2)}(\mathrm{Re}_L^*)\ln(2)^2 - 0.636\,\mathrm{Re}_L^{*0.762}, \tag{C4}$$

where γ is the Euler constant, $E_1(x) = \int_x^\infty \frac{e^{-t}}{t} dt$ is the exponential integral function, and here $\mathrm{Re}_L^* = \rho|\mathbf{U}|L/(2\mu)$. One may observe that $|\mathbf{U}|\cos\theta = U_p$.

b. Expression of F_q

The expression of F_q can be found in [19] and reads

$$F_q(\mathrm{Re}_L^*, \chi, \theta) = 4\pi\mu|\mathbf{U}|L\sin\theta\left(\frac{B^{(1)}_{\mathrm{Re}=0} + B^{(1)}(\mathrm{Re}_L^*)}{\ln(2\chi)} + \frac{B^{(2)}_{\mathrm{Re}=0} + B^{(2)}(\mathrm{Re}_L^*)}{\ln^2(2\chi)} + \frac{B^{(3)}_{\mathrm{Re}=0} + B^{(3)}(\mathrm{Re}_L^*)}{\ln^3(2\chi)}\right. \tag{C5}$$

$$\left. + \frac{B^{(4)}_{\mathrm{Re}=0} + B^{(4)}(\mathrm{Re}_L^*)}{\ln^4(2\chi)} - \frac{0.568}{\chi^{2/3}\left(\chi - \frac{1}{2}\right)^{1.75}}\right), \tag{C6}$$

where $B^{(1)}_{\mathrm{Re}=0} = 1$, $B^{(2)}_{\mathrm{Re}=0} \approx -0.193$, $B^{(3)}_{\mathrm{Re}=0} \approx 0.214$, $B^{(4)}_{\mathrm{Re}=0} \approx 0.387$ [27], $B^{(1)}(\mathrm{Re}_L^*) = 0$, and

$$B^{(2)}(\mathrm{Re}_L^*) = E_1(\mathrm{Re}_L^*) + \ln(\mathrm{Re}_L^*) - \frac{e^{-\mathrm{Re}_L^*} - 1}{\mathrm{Re}_L^*} + \gamma - 1, \tag{C7}$$

$$B^{(3)}(\mathrm{Re}_L^*) = 2\ln(2)B^{(2)}(\mathrm{Re}_L^*) + B_e^{(3)}(\mathrm{Re}_L^*), \tag{C8}$$

$$B^{(4)}(\mathrm{Re}_L^*) = 3\ln(2)^2 B^{(2)}(\mathrm{Re}_L^*) + 3\ln(2)B_e^{(3)}(\mathrm{Re}_L^*) + B_e^{(4)}(\mathrm{Re}_L^*). \tag{C9}$$

We have $|\mathbf{U}|\sin\theta = -U_q$.

c. Expression of T_r^i

The expression of T_r^i can be found in [19]

$$T_r^i(\mathrm{Re}_L^*, \chi, \theta) = \rho|\mathbf{U}|^2L^3\sin(2\theta)\frac{5\pi}{48\left(1 + \mathrm{Re}_L^{*1.991}\right)^{0.331}}\left(\frac{1}{\ln^2(3\chi)} + \frac{2.244 - 1.813\,\mathrm{Re}_L^{*0.543}}{\ln^3(3\chi)}\right.$$

$$\left. - \frac{3.603 + 8.854\,\mathrm{Re}_L^{*0.538}}{\ln^4(3\chi)} - \frac{14.301(\mathrm{Re}_L^*/\chi)^{0.448}}{\ln^5(3\chi)}\right). \tag{C10}$$

One may note that $|\mathbf{U}|^2\sin(2\theta) = -2U_pU_q$.

d. Expression of T_r^Ω

An expression for the resisting torque due to the particle rotation can be found in Pierson *et al.* [18] and may be expressed as

$$\begin{aligned} T_r^\Omega = &-\frac{-\pi\mu\Omega_r L^3}{3}\left[\frac{1}{\ln(2\chi)} + \frac{1}{\ln^2(2\chi)}\left(\frac{11}{6} - \ln 2 + f(\chi, \mathrm{Re}_\Omega^*)\right)\right. \\ &+ \frac{1}{\ln^3(2\chi)}\left(\frac{161}{36} - \frac{\pi^2}{12} - \frac{11}{3}\ln 2 + (\ln 2)^2\right) + \frac{1}{\ln^4(2\chi)}\left(1 - \frac{1}{(2\chi)^{1.2}}\right)^5\left[-\frac{5}{4}\zeta(3) + \frac{1033}{72}\right. \\ &\left.\left. - \ln^3(2) + \frac{11}{2}\ln^2(2) - \frac{161}{12}\ln 2 - \pi^2\left(\frac{11}{24} - \frac{1}{4}\ln 2\right)\right]\right], \end{aligned} \tag{C11}$$

with $f(\chi, \mathrm{Re}_\Omega^*) = 0.018\chi^{2.3}\mathrm{Re}_\Omega^{*0.9}$ and $\mathrm{Re}_\Omega^* = \rho|\mathbf{\Omega}|D^2/\mu$.

2. Long rods: $\chi > 30$

For sufficiently long rods [12], expressions for the loads are accurate. In the following, we present the Khayat and Cox [12] expression, still making use of the linearization proposed by Ref. [28] for the forces. Also we make use of the $1/\ln\chi$ original expansion proposed by Khayat and Cox [12] rather than the $1/\ln(2\chi)$ expansion.

a. Expression of F_p

$$F_p(\mathrm{Re}_L^*, \chi, \theta) = \frac{-2\pi\mu|\mathbf{U}|L\cos\theta}{\ln\chi}\left(1 - \frac{A^{(2)}(\mathrm{Re}_L^*) - 4\ln 2 + 3}{\ln\chi}\right)^{-1}. \tag{C12}$$

b. Expression of F_q

$$F_q(\mathrm{Re}_L^*, \chi, \theta) = \frac{4\pi\mu|\mathbf{U}|L\sin\theta}{\ln\chi}\left(1 - \frac{B^{(2)}(\mathrm{Re}_L^*) + 1/2 - \ln 4}{\ln\chi}\right)^{-1}. \tag{C13}$$

c. Expression of T_r^i

$$T_r^i(\mathrm{Re}_L^*, \chi, \theta) = -\mu U L^2 \frac{\pi}{2}\left(\frac{1}{\ln\chi}\right)^2 \{\cos\theta[P(X) - Q(X) + P(Y) - Q(Y)] + P(Y) - P(X)\}\sin\theta, \tag{C14}$$

with $Q(x) = \frac{E_1(x)+\ln(x)+\gamma}{x}$, $P(x) = \frac{2}{x}(1 + \frac{e^{-x}-1}{x})$, $X = \mathrm{Re}_L^*(1 - \cos\theta)$, and $Y = \mathrm{Re}_L^*(1 + \cos\theta)$.

d. Expression of T_r^Ω

Since to the best of our knowledge there is no expression for this torque for finite inertia effect and very long fibers, we make use of expression (C11) neglecting the inertial correction f.

[1] M. Poulain, M. J. Mercier, L. Brach, M. Martignac, C. Routaboul, E. Perez, M. C. Desjean, and A. Ter Halle, Small microplastics as a main contributor to plastic mass balance in the north atlantic subtropical gyre, Environ. Sci. Technol. **53**, 1157 (2018).

[2] K. Gustavsson, M. Sheikh, D. Lopez, A. Naso, A. Pumir, and B. Mehlig, Effect of fluid inertia on the orientation of a small prolate spheroid settling in turbulence, New J. Phys. **21**, 083008 (2019).

[3] K. Gustavsson, M. Sheikh, A. Naso, A. Pumir, and B. Mehlig, Effect of particle inertia on the alignment of small ice crystals in turbulent clouds, J. Atmos. Sci. **78**, 2573 (2021).

[4] G. K. Batchelor, Slender-body theory for particles of arbitrary cross-section in stokes flow, J. Fluid Mech. **44**, 419 (1970).

[5] R. Cox, The steady motion of a particle of arbitrary shape at small reynolds numbers, J. Fluid Mech. **23**, 625 (1965).

[6] M. Howe, On the force and moment on a body in an incompressible fluid, with application to rigid bodies and bubbles at high and low reynolds numbers, Q. J. Mech. Appl. Math. **48**, 401 (1995).

[7] P. Ern, F. Risso, D. Fabre, and J. Magnaudet, Wake-induced oscillatory paths of bodies freely rising or falling in fluids, Annu. Rev. Fluid Mech. **44**, 97 (2012).

[8] S. Kim and S. J. Karrila, *Microhydrodynamics: Principles and Selected Applications* (Courier, 2013).

[9] M. Loewenberg, Stokes resistance, added mass, and basset force for arbitrarily oriented, finite-length cylinders, Phys. Fluids **5**, 765 (1993).

[10] J. K. Kabarowski and A. S. Khair, The force on a slender particle under oscillatory translational motion in unsteady stokes flow, J. Fluid Mech. **884**, A44 (2020).

[11] C. t. Lawrence and S. Weinbaum, The unsteady force on a body at low reynolds number; the axisymmetric motion of a spheroid, J. Fluid Mech. **189**, 463 (1988).

[12] R. Khayat and R. Cox, Inertia effects on the motion of long slender bodies, J. Fluid Mech. **209**, 435 (1989).

[13] S. I. Rubinow and J. B. Keller, The transverse force on a spinning sphere moving in a viscous fluid, J. Fluid Mech. **11**, 447 (1961).

[14] P. M. Lovalenti and J. F. Brady, The hydrodynamic force on a rigid particle undergoing arbitrary time-dependent motion at small reynolds number, J. Fluid Mech. **256**, 561 (1993).

[15] R. Newsom and C. Bruce, The dynamics of fibrous aerosols in a quiescent atmosphere, Phys. Fluids **6**, 521 (1994).

[16] A. Roy, R. J. Hamati, L. Tierney, D. L. Koch, and G. A. Voth, Inertial torques and a symmetry breaking orientational transition in the sedimentation of slender fibres, J. Fluid Mech. **875**, 576 (2019).

[17] M. Shin, D. L. Koch, and G. Subramanian, A pseudospectral method to evaluate the fluid velocity produced by an array of translating slender fibers, Phys. Fluids **18**, 063301 (2006).

[18] J.-L. Pierson, M. Kharrouba, and J. Magnaudet, Hydrodynamic torque on a slender cylinder rotating perpendicularly to its symmetry axis, Phys. Rev. Fluids **6**, 094303 (2021).

[19] N. Fintzi, L. Gamet, and J.-L. Pierson, Inertial loads on a finite-length cylinder embedded in a steady uniform flow, Phys. Rev. Fluids **8**, 044302 (2023).

[20] F. Cabrera, M. Z. Sheikh, B. Mehlig, N. Plihon, M. Bourgoin, A. Pumir, and A. Naso, Experimental validation of fluid inertia models for a cylinder settling in a quiescent flow, Phys. Rev. Fluids **7**, 024301 (2022).

[21] G. Mougin and J. Magnaudet, The generalized kirchhoff equations and their application to the interaction between a rigid body and an arbitrary time-dependent viscous flow, Int. J. Multiphase Flow **28**, 1837 (2002).

[22] M. Kharrouba, Etude analytique et numérique des efforts s'éxerçant sur des particules cylindriques allongées, Ph.D. thesis Toulouse University, 2020.

[23] M. S. Howe, *Hydrodynamics and Sound* (Cambridge University Press, 2006).

[24] H. Lamb, *Hydrodynamics* (At The University Press, 1953).

[25] C. Toupoint, P. Ern, and V. Roig, Kinematics and wake of freely falling cylinders at moderate reynolds numbers, J. Fluid Mech. **866**, 82 (2019).

[26] V. Dabade, N. K. Marath, and G. Subramanian, Effects of inertia and viscoelasticity on sedimenting anisotropic particles, J. Fluid Mech. **778**, 133 (2015).

[27] M. Kharrouba, J.-L. Pierson, and J. Magnaudet, Flow structure and loads over inclined cylindrical rodlike particles and fibers, Phys. Rev. Fluids **6**, 044308 (2021).

[28] D. Lopez and E. Guazzelli, Inertial effects on fibers settling in a vortical flow, Phys. Rev. Fluids **2**, 024306 (2017).

[29] T. Bhowmick, J. Seesing, K. Gustavsson, J. Guettler, A. Pumir, B. Mehlig, Y. Wang, and G. Bagheri, Inertial angular dynamics of non-spherical atmospheric particles, arXiv:2303.04299.

[30] A. Wachs, A. Hammouti, G. Vinay, and M. Rahmani, Accuracy of finite volume/staggered grid distributed lagrange multiplier/fictitious domain simulations of particulate flows, Comput. Fluids **115**, 154 (2015).

[31] M. Rahmani and A. Wachs, Free falling and rising of spherical and angular particles, Phys. Fluids **26**, 083301 (2014).

[32] A. Seyed-Ahmadi and A. Wachs, Dynamics and wakes of freely settling and rising cubes, Phys. Rev. Fluids **4**, 074304 (2019).

[33] J.-L. Pierson, F. Auguste, A. Hammouti, and A. Wachs, Inertial flow past a finite-length axisymmetric cylinder of aspect ratio 3: Effect of the yaw angle, Phys. Rev. Fluids **4**, 044802 (2019).

[34] A. S. Khair and N. G. Chisholm, A higher-order slender-body theory for axisymmetric flow past a particle at moderate reynolds number, J. Fluid Mech. **855**, 421 (2018).

[35] D. Fabre, P. Assemat, and J. Magnaudet, A quasi-static approach to the stability of the path of heavy bodies falling within a viscous fluid, J. Fluids Struct. **27**, 758 (2011).